FACULTY
OF MATHEMATICS
AND PHYSICS
Charles University

HABILITATION THESIS

From the individualities to the ensemble properties

(the road to protein corona)

Mgr. Anna Fučíkova, Ph.D.

Biophysics, chemical and macromolecular physics

Prague 2025

From the individuality to the ensemble properties

(the road to protein corona)

Contents

Preface 2

1. Introduction: Motivation of the presented research 3

2. Atomic force microscopy and its macro counterparts' methods 6

   2.1 History and basic principles of atomic force microscopy 6

   2.2 Young modulus 9

   2.3 Adhesion Force 14

   2.4 Wettability 15

   2.5 Other parameters achievable by AFM 19

3. Experimental setup 21

4. Overview of the results 25

5. Conclusion and outlook 34

6. List of abbreviations: 35

7. References 36

8. Statement of the author's contribution to the publications 42

9. Appendix: Collection of publications 43

Note: The author used Grammarly, an AI-powered language tool, to improve the clarity and grammar of the written text.

From the individuality to the ensemble properties

(the road to protein corona)

Preface

In this habilitation thesis, I present a collection of 12 papers and one patent, authored or co-authored by me, published in internationally recognized, peer-reviewed journals from 2014 to 2024.

The thesis is organized as follows: In the introduction, Chapter 1, I present what motivated me to do the research described here. Chapter 2 summarizes how the study of interactions between nanoparticles and nanomaterials can be approached using atomic force microscopy (AFM), including its limitations. I also try to explain what complementary macro/ensemble methods can give us with respect to the nanoscale. In Chapter 3, I describe our experimental setup. Chapter 4 contains an overview of the obtained results, which are grouped into four connected topics. The original papers attached to this thesis are in Chapter 9. Chapter 5 contains the conclusion and the outlook for future work. References are listed in Chapter 7, and in Chapter 8, I outline my personal contributions to the research.

This work would not be possible without my more than 170 co-authors and colleagues. I would like to particularly thank Prof. Jan Valenta, Prof. Ivan Pelant, and Prof. Marie Hubalek Kalbačová, who helped me to start my scientific career, and we continue to collaborate to this day. I would also like to thank my postdoctoral adviser, Prof. Jan Linnros, and his group from KTH Stockholm, who gave me great freedom of work, and I spent two great years there. Also, I would like to thank my students who joined me on the scientific route, and I have had the honour of guiding them during their studies.

I would also like to thank the Neuron Foundation for the Grant Impuls financial support I received in 2015 and the following support from Dalibor Dedek. I want to thank the Czech Grant Agency for their support with the junior GACR 2018-2020 grant 18-07977Y and the GACR 2024-2026 grant 24-11110S. Last but not least, I would like to thank Helena Vagnerova for the great opportunity to attend the “Hidden No More” 2018 IVLP program in the US.

Finally, I would like to thank my life partner, Tomas, and my whole family and friends for supporting me on the scientific and life route.

1. Introduction: Motivation of the presented research

The variety of nanostructures available to us and surrounding us today is enormous [1], [2]. The use of nanomaterials is very extensive because of the unique properties of nanoparticles (NPs) arising from their nanometre dimensions. These materials find applications across numerous fields, including solid-state physics, chemistry, engineering, molecular biology, medicine, and interdisciplinary cross-cutting technologies, taking advantage of new and unusual properties of nanomaterials to construct new structures, materials, and devices. The NPs can already be found in many products in the common household [3].

Already during my Ph.D., I learned that it is necessary to study the properties of individual NPs in order to explain the behaviour of the ensemble [4]. I started with the optical characterization of silicon nanocrystals (Si-NCs) and studied their interaction with the biological environment. The results we obtained were promising, but even then, I had noticed that we sometimes had problems matching the physical macro-characteristics of Si-NCs to the interaction with the biological environment. Generally, the individual batches of Si-NCs and other NPs appeared identical (within measurement error) according to the mass/bulk characterization methods, but they behaved differently in the biological environment. For example, NPs from one synthesis batch were biocompatible, whereas NPs from the other synthesis batch showed significant cytotoxic reactions in the biological test. Yet, they were evaluated to be identical by the macro-characterization techniques. Our article [5] later explained this phenomenon in our case: the main issue lies in the fact that current macro-characterization methods cannot detect subtle variations within NP ensembles, so we did not catch the problem of the slight difference in the surface passivation between the batches.

Despite more than 30 years of NP and quantum dot research, our knowledge about their behaviour in the biological environment is very limited. NPs can easily penetrate into the human body [6], [7], and are more biologically active and chemically reactive than larger particles, mainly due to their greater surface-to-volume ratio. Moreover, they can persist in various zones in the living organism or the environment and accumulate there [8], [9], [10], [11]. The first scientific studies are emerging, indicating that NPs are more harmful than previously anticipated [12], [13], [14], [15], [16], [17]. NPs are even associated with so-called civilization diseases [18], [19], [20]. Even in the highly cited articles, the scientists admit that there are considerable gaps in their knowledge about the behaviour of NPs in the biological environment [13]. The main challenges in NP research are that the toxicity and chemical reactivity of these nanomaterials are studied by outdated methods [21], [22], [23], which were developed for molecules and do not work as anticipated on NPs. If we want to know, for example, their cytotoxicity, then there is a problem, since standard viability test kits used in medicine tend to react with bare NPs, giving false negative/positive results [22], [24], [25], [26], [27]. The toxicity of NPs made of toxic elements is, to a certain level, expected. Still, it has been shown that material that is not toxic in the bulk form can be toxic when it is in the form of NPs [23], [28], [29], primarily due to their sharp shape or enhanced chemical reactivity.

A significant role in the NP destiny in the living organism is the primary interaction with the biological environment. Once any nanomaterial is introduced into a living organism, the proteins and present molecules in the environment tend to cover it and create a so-called protein corona

[30], [31], [32], [33] (see Fig. 1), as also studied in our work [34], [35]. Even though the NP nanomaterial from which the NP is made is nontoxic, its protein corona can cause secondary toxicity via inflammatory reactions [36], [37]. This secondary inflammation is mainly connected to structural changes of proteins in the protein corona. Such changes in protein structure are more often associated with nanoparticles with positive zeta-potential[38], [39], but not always (zeta-potential characterizes surface charge on the nanoparticle; it is the potential difference between the dispersion medium and the stationary layer of fluid attached to the dispersed NP).

Although the zeta potential of NPs plays a significant role in their interactions with biological environments and proteins, other parameters beyond surface charge also influence nanoparticle–protein interactions. As previously mentioned, these include chemical reactivity and the high surface-to-volume ratio of NPs. Additionally, factors such as adhesivity, the chemical composition of the NP core and surface, and various other physicochemical properties, including shape, contribute to these interactions. Once the protein corona is formed, it is the corona that determines the destiny [32], [36], [40] of an NP in a living organism since the organism does not interact primarily with the NP itself but with the surface layer of the NP - in this case, proteins and molecules in the corona. The protein corona can also have a beneficial effect on the NP destiny, since if properly covered, it can hide the NP from the immune system and bypass it. We can even target the NP more specifically and prevent it from early retention from the living organism, as summarized in[33] and shown in Fig. 1.

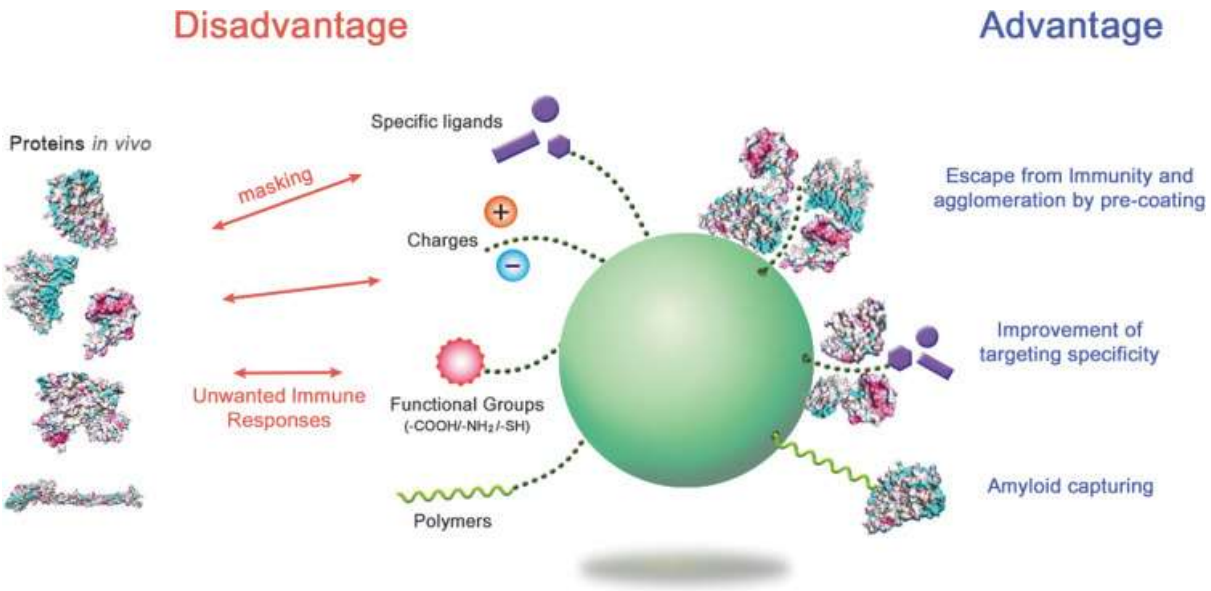

Figure 1: Protein corona formation on nanoparticle (taken from[33])

To reveal the principles and science behind the formation of protein corona, we needed to have more information about the studied NP than is supplied by the manufacturer. Therefore, I started to manufacture the NP myself to have better control over the sample preparation and have all the synthesis parameters. I also performed characterization of the NPs by various ensemble methods, but even that did not help enough to explain the variance in behaviour in the biological environment. Therefore, I went for a postdoc at KTH in Stockholm to improve my chemistry knowledge and skills. In there, I synthesized silicon nanocrystals with a core-shell structure, which have had the narrowest linewidth ever published [41], [42], and I patented the procedure by myself [43], [44]. I needed several measurement and characterization methods to unveil the

science behind the formation of these ultranarrow-emitting NP and their optical properties. I approached the sample from both single dot and ensemble levels to reveal the principles as summarized in publications [41], [42], [43], [44].

Upon my return to Charles University, it was clear that the multiview methodology approach, including ensemble and single nanoparticle approach, is necessary for studying any nanomaterial since it is the little nuances in nanomaterials properties that are not accessible with ensemble measurements that are crucial in decoding their sometimes striking erratic behaviour of the ensemble at the macroscale, which on the end is attributed to nano-properties which have been omitted due to our incapacity to access them with ensemble/macro measurement since the difference between the samples was hidden in the measurement error of the macro measurement.

Our primary tool for studying the behaviour of NPs and nanomaterials at the nanoscale is atomic force microscopy; our setup is described in Chapter 3 (Experimental setup). In the next chapter, we will summarize the abilities and limits of atomic force microscopy to characterize nanomaterials and their macro counterparts.

In this work, I tried to summarize our knowledge of how to access the nano-properties of samples.

2. Atomic force microscopy and its macro counterparts' methods

2.1 History and basic principles of atomic force microscopy

The atomic force microscope (AFM) is the primary tool used in this thesis, so I would like to briefly mention its history, principles of measurement, and technical limits.

The AFM was invented at the IBM company around 1985, and the first publication summarizing this invention was by G. Binnig, C. F. Quate, and Ch. Gerber in 1986 [45].

The first version of AFM consisted of the scanning tunnelling microscope (STM) (which was invented in 1981-1982 by G. Binnig and H. Roher) tunnelling probe, which served as a readout tool of the cantilever position (as shown in Fig. 2); this device was capable of measuring in the air with a lateral resolution of 3 nm and vertical resolution of around 0,1 nm.

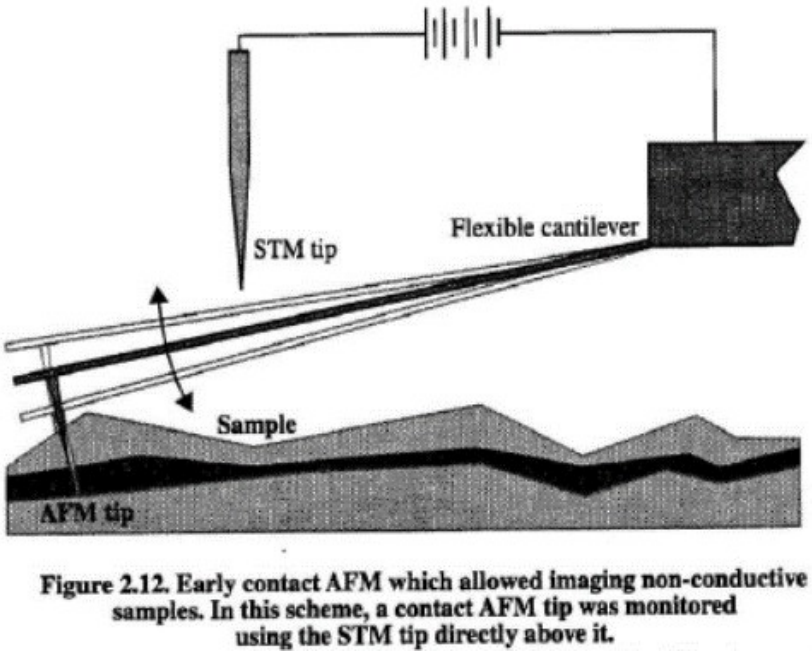

Figure 2: First device capable of measuring atomic forces in air[45] based on a scanning tunnelling microscope.

A cantilever is a small silicon wafer, typically measuring 100–250 µm in length and 15–60 µm in width. On one end of the cantilever is a tip, usually a conical probe with a length of approximately 1-20 µm, with a spherical tip end that has a radius of 1 nm or larger. The variation of cantilever dimensions changes its stiffness, which is presented as spring constant (N/m), ranging from 0.05 N/m to 200 N/m. The range of cantilever parameters and their tips is quite broad, so one can find specific cantilevers for a given application (a few examples are shown in Fig. 3). They can even have a triangular shape to have a very low spring constant, which is necessary for biological measurement. The cantilevers can also be coated with various layers to improve their conductivity, reflectivity, durability, etc.

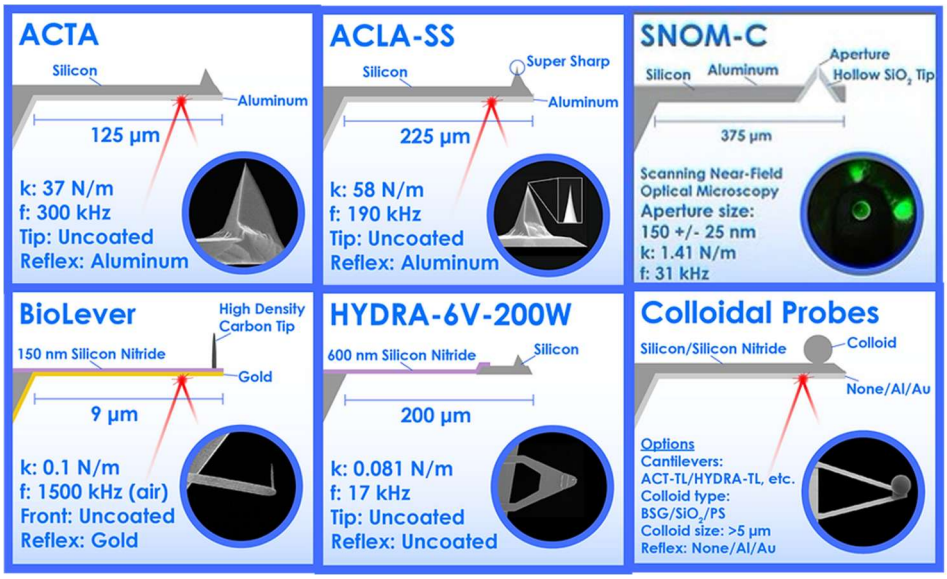

Figure 3: Examples of different cantilevers and their geometries (taken from www.appnano.com). ACTA cantilever is suitable for noncontact measurement and has a tip with a diameter of 8 nm. ACTA-SS is a version of ACTA with a super sharp tip of 1-2 nm in diameter. SNOM-C allows the measurement of the sample's topography and allows the taking of luminescence from a limited spot on the sample. BioLever enables the detailed measurement of biological samples and works within the environment of biological fluids. Hydra-6V-200W type cantilevers are soft and suitable for biological measurements with detail. Colloidal probes are ideal for nanomechanical measurements such as Young's modulus; their tip diameter can vary from a few nm to a few µm.

The cantilevers now enable a broad spectrum of applications, ranging from simple topography measurements to the nanomechanical, chemical, and physical characterization of samples [46], [47].

The reading of the cantilever position with the STM probe on the first AFM device greatly limited the selection of samples that could be measured; they needed to be relatively flat in the range of a few nm. For a short time, there was an idea to use a surface profiler/profile stylus (based on the invention of 1929 by Schmalz [48]), on top of a cantilever as a position reader. This device was based on a small mirror on the cantilever that reflected light from a light source and aimed it at photographic film. This principle was quickly abandoned; in a new approach, a laser (first developed in the 1960s) was used as the light source, and the top surface of the cantilever served as a mirror. The first commercially available AFM with an embedded laser source and light detector became available in 1989. The standard AFM configuration for topography measurement with the currently used devices is shown in Fig. 4.

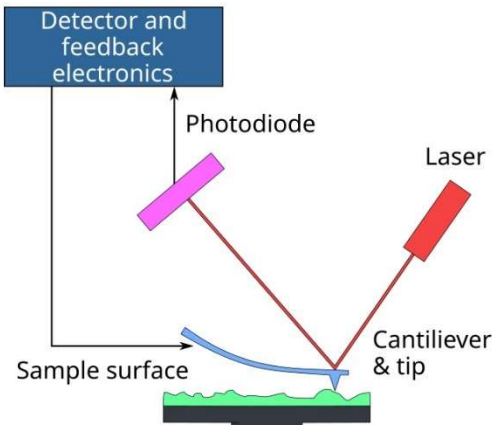

Figure 4: Standard AFM microscope setup.

The basic principle of AFM has remained essentially unchanged since 1989. The cantilever is mounted on a piezoelectric element, which enables highly precise movement along the Z-axis, with displacements ranging from fractions of a nanometre to a few micrometres (in our case, the maximal range of our piezoelement is 10 µm). The piezo element and cantilever are placed in a part of the AFM device called the AFM head, which typically includes a laser, a photodiode, and a holder for the piezo actuator. The AFM head is usually motorized using stepper motors that allow for coarse approach and alignment to the sample.

When the cantilever approaches the sample and comes into contact with or interacts with the sample surface, the interaction causes the cantilever to bend. This cantilever bending changes the path of the laser beam in the AFM head and the position of the laser spot on the photodiode detector. From the position of the laser spot on the photodiode and the device feedback, we can calculate not only the position of the cantilever and, therefore, sample height but also other parameters, as discussed in subsequent chapters.

The precision of the cantilever's position on the Z-axis is usually in Ångstroms (perpendicular to the sample), since this axis is the same as the piezo element's main axis. In contrast, resolution in the X and Y axes is influenced by the geometry and sharpness of the cantilever tip. For the sharpest tips (with radii around 1 nm), the lateral resolution can reach approximately 0.5 nm in optimal conditions, though typical resolution ranges from 1–2 nm. This lateral resolution is affected by tip–sample convolution, tip shape, and the selected imaging mode.

The basic imaging modes are:

- **Contact Mode:** The AFM tip maintains constant contact with the sample surface, and the cantilever's deflection generates the topographic image. This mode is not suitable for samples with a high aspect ratio. Due to the cantilever's direct contact with the sample, it is prone to damage during this measurement, including bending or more problematic bolding the cantilever.
- **AC (Amplitude Modulation) Mode / Tapping Mode:** The cantilever oscillates at or near its resonance frequency, intermittently tapping the sample surface. Changes in amplitude, phase, and frequency are used to create images of sample topography, as well as material properties like viscoelasticity and adhesion.

- **Quantitative Imaging (QI) Mode / PeakForce Tapping:** This mode operates by precisely controlling the force applied at each pixel, generating a force curve at every measured point. This allows quantitative mapping of various mechanical properties such as Young's modulus, adhesion, dissipation, and deformation, with minimal lateral forces, making it ideal for soft and delicate samples.

gAdvanced and Specialized Modes:

- **Force Spectroscopy:** Measures the interaction forces between the tip and sample as a function of their separation. This is crucial for studying single-molecule interactions, cell adhesion, unfolding of proteins, and mechanical properties of materials.

With the AFM, we can also obtain data usually obtainable with STM, with the use of

Electrical Modes:

- Conductive AFM (also known as CAFM) measures local electrical conductivity by detecting current flow through a conductive tip in contact with the sample surface.

- Scanning Tunnelling Microscopy (STM): This technique provides atomic-resolution images based on tunnelling current for conductive samples.

In the following chapters, I will address the parameters that can be obtained using AFM, their limitations, and their macroscopic counterparts.

2.2 Young modulus

The measurement of the mechanical properties of samples differs significantly between the macro- and nanoscale. When measuring the macroscopic Young's modulus of a material, the smallest area from which it can be reliably determined is typically several mm^2 or even cm^2. At the macroscale, we measure ensemble properties of bulk materials over volumes on the order of mm^3 or larger. In contrast, when measuring Young's modulus using AFM, we probe mechanical properties on the scale of several nm^2 to a few hundred nm^2, with indentation depths typically ranging from a few tens to a few hundred nanometres at most. The contrast between macroscale and nanoscale measurements of Young's modulus can be illustrated using hydrogels (such as agar gel), which are composed of interwoven fibers containing water in small pockets formed by the fibre network. At the macroscale, compressing the gel involves deforming both the fibre network and the water within it. In contrast, at the nanoscale—such as in AFM measurements—we probe down to individual fibers, and the surrounding water is displaced. As a result, a single fibre within the gel can exhibit a Young's modulus several orders of magnitude higher than that of the entire sample measured at the macroscale. Additionally, Young's modulus of individual fibers can vary depending on factors such as their length and degree of crosslinking, etc. [49].

Nanomechanical properties, particularly Young's modulus and wettability, are critically important for cell interactions with nanomaterials. Cells have finger-like protrusions on their surface; in literature, they are called filopodia [50], which act as sensory and exploratory structures. The filopodia are usually 30-100 nm in diameter and several hundred nanometres long. Therefore, biologically relevant nanomechanical properties of a material should be measured over areas ranging from a few tens to a few hundred nm^2.

At the macroscale, the Young's modulus *(E)* describes the elastic properties of a material under tension or compression. It is defined as the ratio of tensile stress (σ) to tensile strain (ε). Stress is the force applied per unit area *(σ = F/A),* and strain is extension per unit length *(ε = dl/l)*.

Equation 1

$$E = \frac{\sigma}{\varepsilon}$$

The equation assumes that the measured area is at the macroscale and that the size of individual molecules or nano-fibres is several orders of magnitude smaller than this area. It also assumes that the material is significantly thicker than the compressed region or much taller than the compressing probe.

The Young's modulus at the nanoscale can be estimated by AFM and is calculated from the so-called force-distance curve (see Fig. 5). To obtain accurate force–distance curves for Young's modulus calculation, the cantilever spring constant should be appropriately selected to match the expected stiffness of the sample. If the cantilever is too soft, it may bend too much during measurements, leading to low force sensitivity and poor resolution of the sample's mechanical properties. Conversely, if the cantilever has too high a spring constant, the sample may not provide enough resistance, and the cantilever may not deform the sample enough to obtain accurate measurements; it may even cut the sample easily as a knife cuts butter and create a permanent indentation in the sample. On the other hand, permanent indentation can be used to calculate surface stiffness for hard samples. Similarly, hardness can be obtained from the resistance of the sample to the cantilever penetration. These techniques are usually applied tostudy thin films and coatings, but neither of them is standardly used in biological experiments.

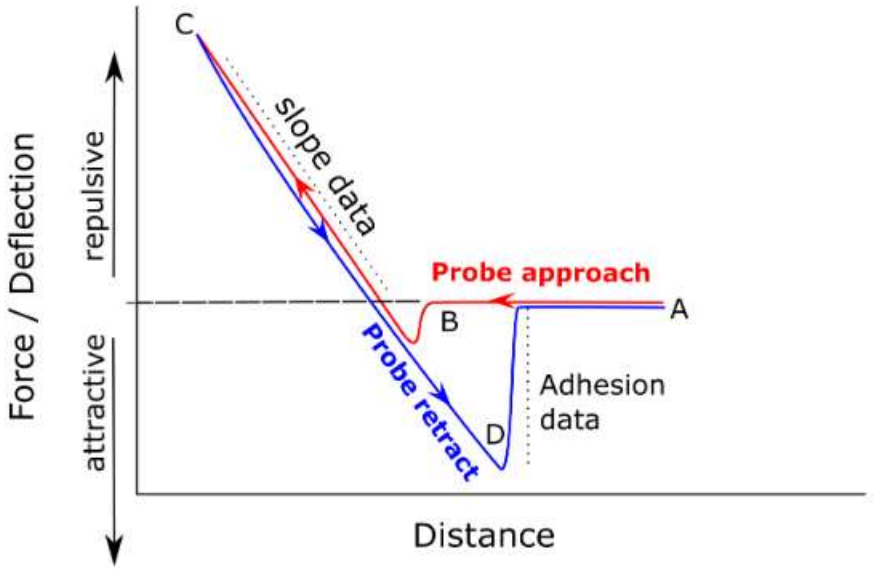

Figure 5: AFM force-distance curve (taken from [51]) measured in air.

The red curve in Fig. 5, named “Probe approach,” shows the force-distance curve and the cantilever path as it approaches the sample; it is also known as a trace curve. The “Probe retract” curve in blue shows the cantilever path as it moves away from the sample and is referred to in the literature as a retrace curve.

When we look at the red curve in Fig. 5, we see that the cantilever begins moving from a position high above the sample at point A and approaches the sample until it reaches point B, which is sometimes referred to as the “contact point.” We can see that at point B, there is a sudden move of the cantilever towards the sample; this move is described in the literature as a “snap-in” move. The snap-in event is caused by the presence of thin water layers—typically several nanometres thick—on both the sample and cantilever surfaces under standard conditions in air. The thickness of these surface water layers depends on the sample/cantilever wettability and, of course, also the environmental humidity [52]. The snap-in move is, therefore, caused by the Van der Waals attractive forces of the two water layers.

Between points B and C, we are compressing the sample with the AFM cantilever. The Young’s modulus can be calculated from this part of the curve. The depth of cantilever indentation into the sample can be calculated as the distance between point B and C in the x-coordinate (dashed line on Fig. 5).

The cantilever is retracted from the sample between points C and D (point D is sometimes referred to as the pull-off point). As shown in the figure, point D lies farther from the sample than the contact point B. That indicates that the sample sticks or adheres to the cantilever. The adhesive force can be calculated from the distance of point D from the distance line (shown as a dashed line in the picture). At this point, the approach and retract curves of the cantilever overlap/meet.

Force distance measurements performed in air are affected by the presence of surface water layers, which causes the contact point (point B) to appear higher than the actual sample surface. Since accurate identification of the contact point is crucial for fitting the correct Young’s modulus, it is beneficial to perform the measurement with the sample submerged in water. In liquid, van der Waals forces and the resulting snap-in effect are minimized, allowing more accurate determination of the actual contact point and the whole nanoindentation curve.

We need to know the cantilever parameters accurately in order to fit the nanoindentation curve and determine Young's modulus correctly. In theory, the spring constant and cantilever geometry are known from the manufacturer. However, in practice, both the shape and spring constant can vary within the same batch of cantilevers, with spring constant variations typically within the few tenths of a percent. The actual spring constant of individual cantilevers is easily accessible by automated calibration measurement by the AFM [53]. Optimally, the shape of the cantilever should also be measured prior to the AFM measurement. This can be done, for example, by scanning electron microscopy (SEM) since, as we can see in Fig. 7, the shape of the cantilever tip plays a crucial role in selecting the right model for calculating Young’s modulus at the nanoscale. One drawback of measuring cantilevers by SEM is that, due to the nature of SEM imaging, the cantilever gets covered by a carbon layer (the main source is organic impurities, which are decomposed by the electron beam). This can alter not only its shape but also its properties, such as wettability. Additionally, increased handling of the cantilever increases the risk of damage from improper manipulation. It is also important to note that the shape of the cantilever tip can change during an AFM measurement of the sample. Therefore, the cantilever's spring constant and its tip's shape should be measured before and after the measurement to reveal if there was

any cantilever deformation caused by the measurement, which would affect the fitting of the force-distance curve.

One example of such cantilever changes during the measurement is shown in Fig. 6.

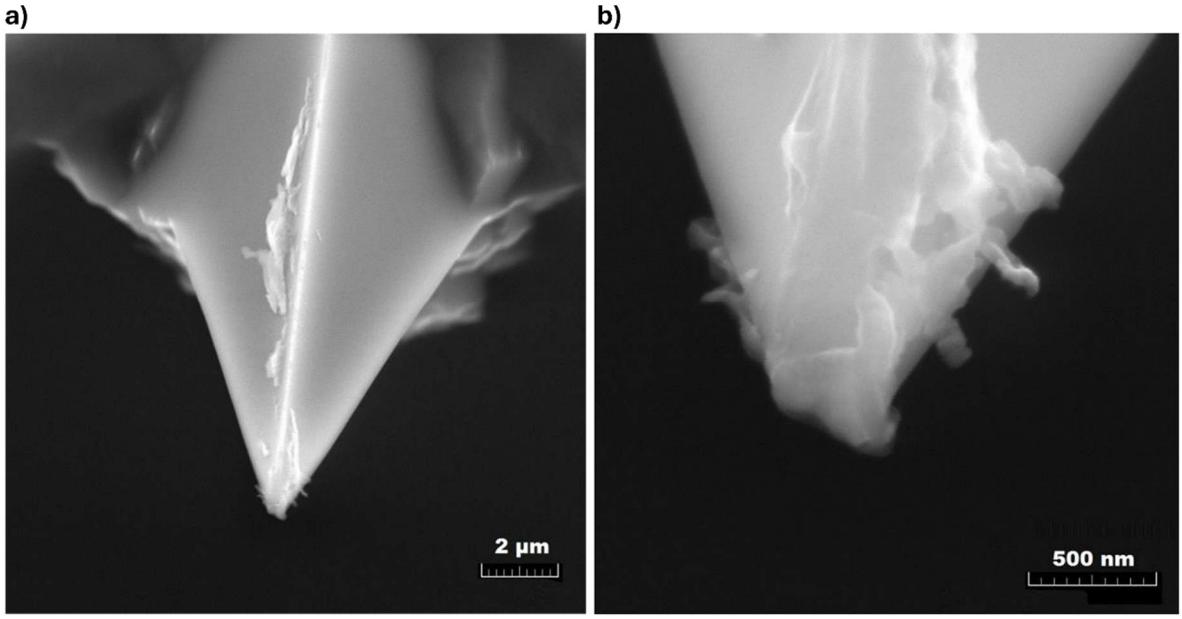

Figure 6: SEM image of a cantilever measured after AFM measurement of soft hydrogels, a) and b) the same cantilever with different magnification (taken from [54]).

As one can see in Fig. 6, which was taken from the bachelor's thesis of T. Hofrichterová[54], which I co-supervised, the cantilever shape was altered during AFM measurement. This deformation significantly complicates the fitting of Young's modulus at the nanoscale. Unlike macroscale measurements, where a universal fitting formula (e.g., Eq. 1) can be applied, nanoscale calculations are more sensitive to parameters such as the cantilever angle and its circularity, which may be unreliable due to cantilever deformation during measurement.

Based on the shape of the cantilever tip and how deeply it indents the sample, we can use either the Hertz or the Sneddon model (see Fig. 7) for fitting Young's modulus from the force-distance curve (see Fig. 5). The Hertz model, which assumes that the tip is a full or half sphere, is appropriate when the indentation depth is smaller than the tip's sphere radius. In contrast, the Sneddon model applies when the indentation is deep enough for the tip shape to approximate a supersharp cone. For indentation depths between these two extremes, the fitting involves a combination of both models, and the Young modulus fitting is therefore complicated [55].

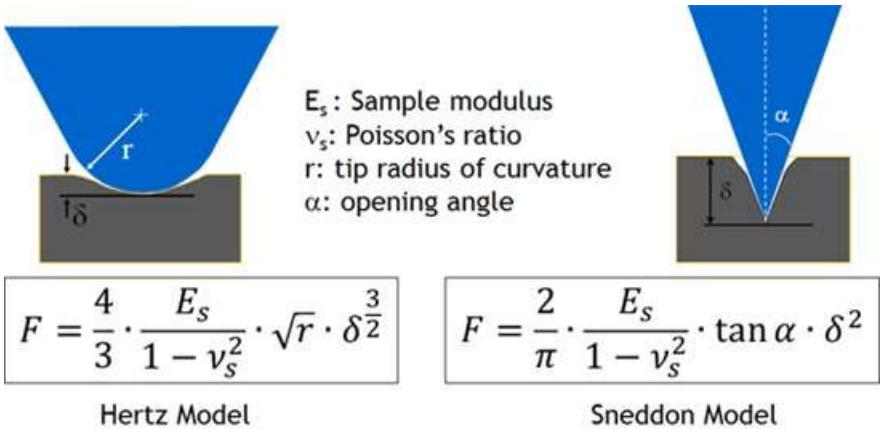

Figure 7: The Hertz and the Sneddon Model for Young modulus fitting at the nanoscale, taken from [56], δ represents indentation dept to the sample.

For accurate fitting of the Young's modulus, it is essential to correctly identify the contact point, which corresponds to the sample surface and defines the zero-distance reference. This is a critical step in Young's modulus fitting [57]. It is important to avoid artifacts during the measurement, such as the snap-in effect in the force–distance curve. For this reason, most Young's modulus measurements at the nanoscale are performed in liquid environments, typically in water, where capillary forces are minimized and snap-in is reduced.

Published Young's modulus values for various materials at the nanoscale remain inconsistent, as the methodologies and theoretical models underlying these measurements are still under development [58], [59], [60], including the use of artificial intelligence[61]and machine/deep learning [62], [63]. For most experiments, it is sufficient to determine the relative difference between the Young's moduli of two nanomaterials, such as how one material compares to another, rather than obtaining their absolute values. This comparative approach is especially used in studying biological systems [64] [65].

One way to achieve a Young's modulus value comparable to that measured at the macroscale is to use a colloidal sphere cantilever tip, where the sphere is glued to the cantilever. This sphere typically has a diameter of several micrometers. However, because these probes must be handcrafted and individually calibrated, their cost is too high for routine use. Also, due to their larger contact area and reduced spatial precision, these probes are often less suitable for high-resolution imaging or nanoscale measurements.

Another possible approach to obtain Young's modulus close to biologically relevant scales is the use of commercial nanoindenters, such as the Hysitron Nanoindenter (now part of Bruker company). These devices indent the sample - usually a metal or macroscale-sized sample - using a hard, pyramidal-shaped tip. They evaluate nanoscale mechanical properties by analysing the resulting indentation spot, which can be as small as several hundred nanometres in diameter.

In addition to hardness measurements, nanoindenter-based techniques enable obtaining elastic modulus, creep, stress relaxation, viscoelastic properties, interfacial adhesion, and fracture toughness characterization at sub-micrometre length scales [66]. However, due to the nature of the measurement process, these instruments are not yet capable of reliably testing extremely soft materials such as living cells or individual proteins.

2.3 Adhesion Force

As shown in Fig. 5, the adhesion force can be obtained from the force-distance curve. It is calculated from the pulling out force from the part of the force-distance curve when the cantilever distances itself from the sample in which it was indented. The adhesion force is important in surface chemistry and bioadhesion [57]. The probed area can be as small as one chemical site or one protein (down to a few nm^2) with typical forces in the range of a few nanonewtons (nN) to micronewtons (µN).

By using a surface-modified cantilever tip with molecules that are selectively bound or attracted to specific surface groups, these measurements can, for example, help identify the locations of individual chemical groups or even proteins [67] or their orientation on the sample surface [57], [68]. Specific interaction, like protein folding [68] or protein-ligand binding under near-physiological conditions in close to in vivo conditions, can be studied [67].

At the macroscale, adhesion is typically measured using mechanical tests such as peel, lap shear, or pull-off tests, which evaluate the force required to separate bonded surfaces [69]. These tests generally require a contact area of several square millimeters or more [70]. The peel test involves peeling one substrate away from another at a constant angle (usually 90° or 180°), and the force required is measured as peel strength (N/m). The pull-off test (also known as the tensile adhesion test) is commonly used for coatings (e.g., paint or protective films) on rigid substrates like metal or concrete. In this test, a loading fixture ("dolly") is glued to the surface, and a perpendicular tensile force is applied until the coating detaches, yielding the tensile adhesion strength (MPa or psi). The lap shear test is used for structural adhesives (such as epoxies) and bonding rigid materials. For the measurement, two overlapping substrates are bonded together and then pulled in shear until failure, providing the shear strength (MPa or psi). Less commonly used is the scratch test, which is applied to thin films and coatings on hard surfaces (like metals or ceramics). A stylus is dragged across the surface under increasing load until the coating delaminates, and the critical load for delamination is recorded. The tape test (also known as the cross-cut or X-cut adhesion test) is often used for paints and coatings. A blade scores the coating in a crosshatch or X pattern, and adhesive tape is applied and then peeled off. A qualitative rating (e.g., 0B to 5B) indicates the amount of coating removed.

When examining adhesion forces in detail, we find that several types of interactions contribute to overall adhesion, and some of these can be distinguished. Chemical adhesion involves the sharing of atoms and electrons between materials through covalent, ionic, or hydrogen bonds. Mechanical adhesion, on the other hand, occurs when one material interlocks with another by filling in surface pores or irregularities. Dispersive adhesion, a form of physisorption, involves van der Waals forces between materials with slight positive and negative charges. Diffusive adhesion typically occurs in soluble materials such as polymers, where one end of a polymer molecule diffuses into another material, leading to adhesion through molecular interpenetration [71]. In work by B. Cappella [72], it was demonstrated that AFM is capable of probing van der Waals forces with high spatial and force resolution. However, determining van der Waals constants from adhesion experiments has limited utility, as it assumes that the solid surfaces remain unchanged upon contact. Given the high pressures beneath the AFM tip in the contact region, this assumption is often invalid [57].

Another major problem in measuring the van der Waals force is the characterization of the geometrical properties of the tip (tip shape) and the sample (roughness), which should be known

prior to the measurement. The measurement itself can also be affected by humidity (change in capillary forces), surface roughness, and even contact time and scanning speed.

In summary, both macroscale and nanoscale adhesion methods aim to quantify how strongly two surfaces adhere, but they differ significantly in scale, mechanisms, measurement techniques, and influencing factors [73]. Due to these scale-dependent effects, the measured adhesion values can vary by several orders of magnitude, even for the same material. At the nanoscale, adhesion is typically measured at the level of single fibre or even molecule-molecule interactions. In contrast, macroscale measurements reflect the collective behaviour of many contact points, surface roughness, and bulk mechanical properties.

2.4 Wettability

Wettability at the macroscale is defined as the tendency of one liquid to spread on or adhere to a solid surface in the presence of other immiscible fluids [74]. The wettability of any material is determined based on the contact angle between the surface and the liquid droplet. In 1936, R. N Wenzel [75] proposed an equation for the apparent contact angle formed by a liquid wetting a rough surface, θ_W, accounting for the influence of surface texture on wettability (see Fig. 8).

$$\cos\theta_{\mathrm{W}} = \bar{\mathrm{r}}\cos\theta_{\mathrm{Y}},$$

Figure 8: contact angle and Wenzel equation [76].

where r̄ is the average roughness ratio, defined as the factor by which roughness increases the solid-liquid interfacial area.

Nomenclature when θ is:

θ=0: perfect wetting,

90° ≤ θ < 180°: low wettability,

θ>150°: surfaces in this range are often referred to as superhydrophobic

It is obvious that for this equation to be physically meaningful, the condition $|\bar{r}\cos\theta Y| \leq 1$ must be satisfied, where θ_Y is the contact angle. The derivation of this equation [75] is similar to that of the Young equation, with the key difference being that the solid–liquid interfacial area is multiplied by the roughness ratio $\bar{r}$. Accordingly, the Wenzel equation describes the relationship

between the apparent contact angle (on a rough surface) and the intrinsic Young contact angle (on a smooth surface), assuming the absence of line tension effects [76].

It has been mathematically demonstrated that, for sawtooth-patterned surfaces, the Wenzel equation accurately predicts the apparent contact angle in the limit where the droplet size is much larger than the characteristic length scale of the surface roughness [76].

This highlights the fact that wettability is a macroscopic parameter: it is typically assessed by placing a droplet (usually ≥ 1 µL) on the surface, photographing the droplet profile, and measuring the resulting contact angle. At the macroscale, the contact angle is standardly measured using a tensiometer. The measured contact angle thus reflects an average over numerous microscopic surface features [77].

In recent years, a new generation of tensiometers has been developed that uses piezo-driven inkjet dispensing technology to deliver droplets as small as 20 picolitres, resulting in droplet diameters of less than 100 µm [78]. While this advancement enables multiple measurements across a single sample and improves spatial resolution, it still does not provide a complete characterization of the surface at biologically relevant length scales or with sufficient statistical sampling for nanostructured surfaces.

On the other hand, at the nanoscale, traditional assumptions used in macroscopic wettability measurements often do not hold. Many engineered surfaces—such as those featuring nanopillars, nanogrooves, or nanodroplets—exhibit behaviour that deviates significantly from classical wetting models, despite fulfilling the macroscopic criterion that the droplet size is considerably larger than the surface roughness.

Wettability at the nanoscale can be effectively characterized using AFM, particularly when traditional macroscopic methods like contact angle goniometry are unsuitable due to surface heterogeneity at the nanoscale or limited sample size. Rather than measuring contact angles directly, AFM assesses surface–liquid interactions through force–distance curves [72]. This is typically done using a liquid-coated AFM tip, a fluid-filled cantilever, or a colloidal probe. As the probe approaches and retracts from the sample surface, the resulting adhesion or pull-off force reflects the surface's wettability—higher adhesion corresponds to more hydrophilic behaviour, while lower adhesion indicates hydrophobicity. In some configurations, capillary forces arising from meniscus formation under humid conditions can also be measured, offering indirect insights into contact angles and surface energy. Colloidal probe AFM, in particular, enables quantification of polar and dispersive surface energy components using functionalized spherical tips. This technique is especially valuable for studying local wettability on nanostructured, biomimetic, or chemically patterned surfaces with nanometre-scale precision. Overall, AFM-based wettability measurements offer a highly sensitive, localized, and non-destructive approach to characterizing surface–liquid interactions at the nanoscale.

The nanostructured surfaces often display superhydrophobicity, a phenomenon commonly referred to as the “Lotus effect” in the literature. This effect arises from the combination of low surface energy materials and hierarchical surface roughness, which together promote high contact angles (≥150°) and low contact angle hysteresis.

The name of this effect was inspired by nature. The real plant lotus leaf (see Fig. 9) is covered with sharp micro- and nanostructured pillars, most of which are coated by a hydrophobic waxy layer (see Fig.9). These pillars are nearly non-wettable. A water droplet barely contacts the underlying solid (see Fig. 10). The lotus leaf is often regarded as a symbol of cleanliness. As shown in Fig. 10,

when dirt particles land on the leaf, water droplets rolling over the nanostructured surface pick up the dirt particles and carry them away. The likelihood of dirt escaping the droplet is extremely low due to minimal solid–solid contact between the particles and the leaf surface.

The effect of superhydrophilicity caused by nanopillars, or more precisely nano-whiskers, is observed, for example, in Salvinia molesta [79], where these nanostructures help the leaf to float on the water. In rice leaves, we observe not only superhydrophilicity due to nanopillar structures but also superwettability thanks to riverbed-like structures [80], and there are more cases like these in nature. These examples illustrate how nature uses hierarchical nano-surface architecture to control liquid behaviour in both hydrophobic and hydrophilic regimes.

This nano-structuring is found not only in plants but also in various living organisms, for example, on the compound eyes [81] of insects or the wings of butterflies [82], springtail legs, etc. In living organisms, the nano-structuring has not only water-repellent properties but also, in many cases, antibacterial ones [83]. One great example is insect wings, such as butterfly wings or dragonfly wings. These wings have on their surface nanopillar structures which, when a bacteria is present on them, rupture the bacteria's membrane [84]. The scientists are starting to manufacture artificial materials with these nature-inspired lotus effect materials and nanopillar structures [85], [86], [87]. In Ing. thesis of M. Černý [88], which I co-supervised, we explored the imprinting of dragonfly wing structures onto a polymer matrix and analyzed their nanostructure using AFM. The imprinted matrix was then used as a stamp for the large-scale production of nano-surfaced materials with antibacterial properties. These nanostructured materials show strong potential in fighting resistant bacterial strains, with promising uses in preventing bacterial growth in hospital water systems and on the surfaces of medical devices [84].

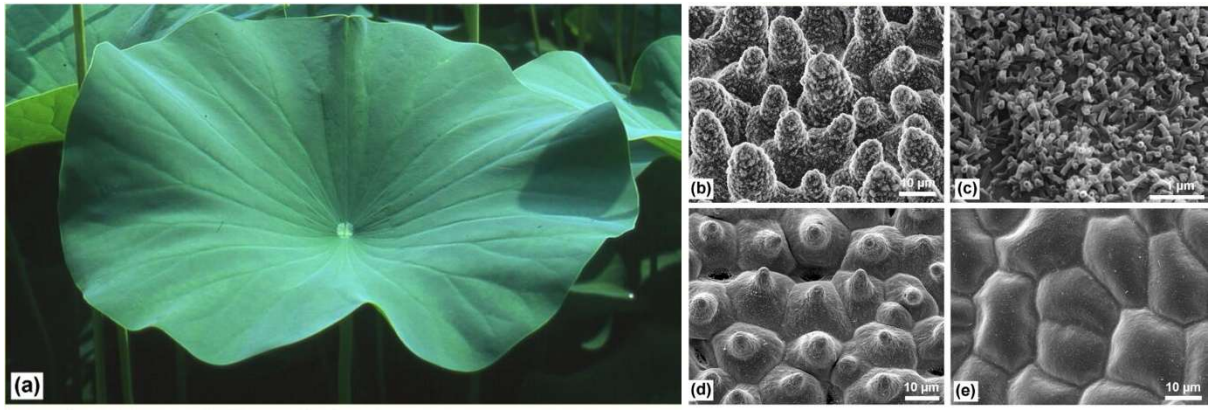

Figure 9: (a) Lotus leaves, which exhibit extraordinary water repellence on their upper side. (b) Scanning electron microscopy (SEM) image of the upper leaf side prepared by 'glycerol substitution' shows the hierarchical surface structure consisting of papillae, wax clusters, and wax tubules. (c) Wax tubules on the upper leaf side. (d) Upper leaf side after critical-point drying. The wax tubules are dissolved, thus the stomata are more visible. Tilt angle 15°. (e) Leaf underside (dried) shows convex cells without stomata (taken from[89]).

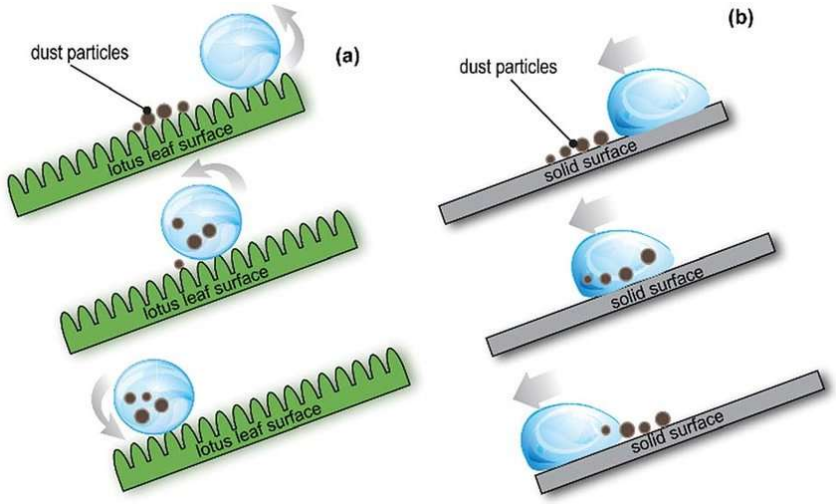

Figure 10: Self-cleaning effect of lotus leaf nanostructure (taken from[90]).

Another example of tailored nano-structuring in combination with surface groups passivation is nicely represented in [91]. The authors prepared a nanodiamond surface with different roughness (1 and 500 nm), where the surface was either terminated with oxygen groups (hydrophilic) or hydrogen (hydrophobic). After 2 days of exposure of the osteoblast cells to these nanostructures, it was observed that the cells adhered and proliferated only on the oxygen-terminated surface.

It is not always necessary to measure wettability; in some cases, it is sufficient to characterize surface properties that affect the macro wettability, such as surface roughness, surface energy mapping by measuring force curves with surface-modified cantilevers, which yield adhesion forces that correlate with hydrophobic or hydrophilic behaviour. Last but not least, we can map mechanical properties like modulus and adhesion, offering us insight into local wetting properties. All these characteristics are measured by AFM on a biologically relevant scale [92], whereas traditional wettability measurements are typically conducted at a much larger (macroscale) level.

We need to keep in mind that the animal cell's contact with the material is provided via filopodia [50], [93], as illustrated in Fig. 11, which is a membrane-enveloped actin filament resembling a finger-like structure. The tip of the finger/filopodia has a diameter in the range of 60-400 nm, depending on the cell type, with a diameter mostly around 100 nm. Filopodia are involved in numerous cellular processes, including cell migration, wound healing, adhesion to the extracellular matrix, guidance towards chemoattractants, neuronal growth-cone pathfinding, and embryonic development. In contrast, the entire animal cell is usually in the size range of 5-20 µm in diameter. This means we are interested in parameters such as wettability and surface features at the nanoscale, on areas three orders of magnitude smaller than current macroscopic tensiometers can accurately measure [77]. The animal cell interacts with nanostructures of a similar size to the filopodia on the sample surface. At the same time, the surface must also provide sufficient mechanical support; otherwise, the cell membrane may experience increased mechanical stress, which could potentially lead to membrane rupture [94].

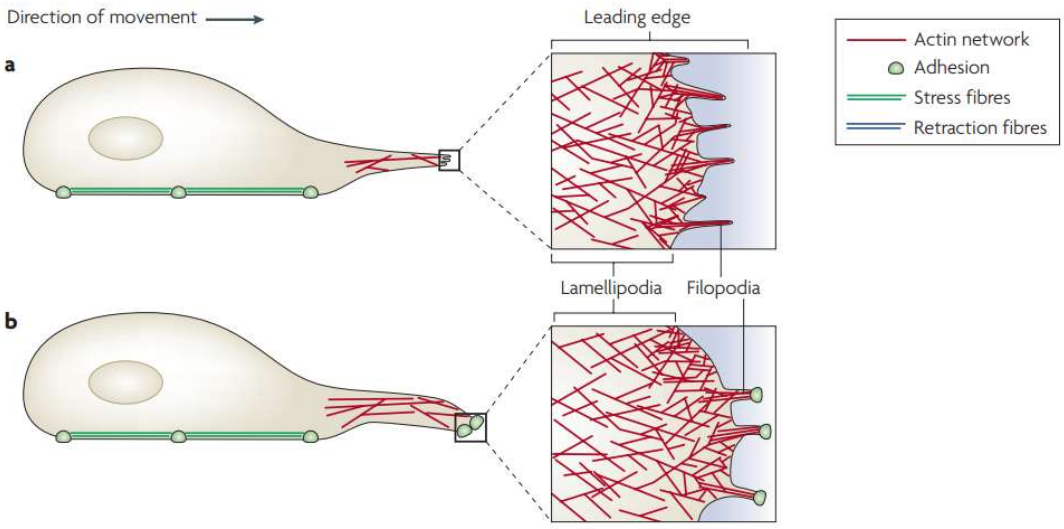

Figure 11: Cel which l migration is dependent on different actin filament structures. a) Motility is initiated by an actin-dependent protrusion of the leading edge, which is composed of lamellipodia and filopodia. These protrusive structures contain actin filaments, with elongating barbed ends oriented towards the plasma membrane. b) During cellular extension, new adhesions with the substratum are formed under the leading edge [93].

For the primary interaction of cells with any sample, surface nano-roughness and chemical surface groups are crucial; both parameters are closely connected with sample wettability. The Young modulus is also important, but mainly in the sense that the surface gives enough support to the cell and prevents it from sinking in. In a general approach, we do not need Young's modulus for cell-material interaction, and all other above-mentioned parameters are mirrored in adhesion forces, which can be easily measured by atomic force microscopy by measuring the force-distance curve (see Fig. 5).

2.5 Other parameters achievable by AFM

Viscoelasticity

AFM can measure viscoelasticity through techniques that measure material's elastic and viscous responses to cantilever indentation at the nanoscale. They can be obtained by measuring force–distance (force spectroscopy) curves, where time-dependent behaviour such as hysteresis, creep, or stress relaxation can be observed during loading and unloading cycles. Dynamic methods such as force modulation or AFM-based dynamic mechanical analysis can be used for more quantitative analysis. We apply oscillatory forces to the sample while monitoring the phase and amplitude response. This allows calculation of the storage modulus (elastic behaviour), loss modulus (viscous behaviour), and the loss tangent, which indicates the degree of viscoelasticity. Additionally, techniques like contact resonance AFM and multifrequency (also known as AM-FM) modes provide enhanced sensitivity to viscoelastic properties by detecting shifts in cantilever resonance or simultaneously mapping stiffness and dissipation [95]. The resolution of these methods reaches down to a few nm^2, and standardly, the samples are soft ones such as polymers, hydrogels, and biological tissues. The measured data often require advanced modelling techniques to extract reliable parameters [96].

Viscoelasticity at the macroscale is commonly measured using Dynamic Mechanical Analysis (DMA), where a material is subjected to a sinusoidal (oscillatory) stress or strain, and the resulting strain or stress response is recorded. From the phase lag between input and output, the storage modulus (elastic component) and loss modulus (viscous component) can be determined, along with the loss tangent (tan δ), which quantifies damping behaviour [97]. The minimal sample zone, which is measured, is at least a few square millimeters for some measurements, but standardly it is around a few 10 nm in diameter. Therefore, we face the same problem as in previous measurements at the macroscale; we measure samples over several contact points in the gel network compared to single-fibre measurements by AFM.

Energy dissipation

The information about energy dissipation can be achieved by measuring tip–sample interactions and analyzing the hysteresis between the approach and retraction segments of force–distance curves. The area enclosed by this hysteresis loop represents the energy lost during the loading–unloading cycle, often due to adhesion, viscoelastic deformation, or interfacial friction. In dynamic modes such as tapping mode, energy dissipation is determined by monitoring changes in the cantilever's oscillation amplitude and phase shift relative to the drive signal. A larger phase lag or reduced amplitude indicates greater energy loss per cycle. These measurements offer nanoscale insights into material properties such as viscoelastic damping, adhesion hysteresis, and surface heterogeneity [98]. Again, the cantilever tip determines the minimal measured sample zone.

At the macroscale, energy dissipation is typically measured using mechanical testing methods such as DMA, as in the case of viscoelasticity, or cyclic loading tests, where a material is subjected to repeated loading and unloading. The resulting stress–strain curve often forms a hysteresis loop, and the area within this loop represents the energy dissipated during one deformation cycle—usually due to internal friction, viscoelastic damping, or plastic deformation. These measurements are essential for understanding the performance of materials under cyclic or dynamic loading, particularly in applications like vibration damping, shock absorption, and material fatigue analysis.

Electrical and STM measurements

The AFM is also capable of electrical and STM-like measurements. Since these modes are not core parts of this work, we mention them briefly in the next chapter, which contains the device description.

3. Experimental setup

I used a broad spectrum of measuring techniques and devices in my research, ranging from advanced optical characterization, including single-dot spectroscopy, to chemical characterization methods such as Fourier transform infrared spectroscopy (FTIR), dynamic light scattering, etc. During my PhD. study, I was responsible for building up a cell maintenance lab, which consisted of a small CO_2 incubator (LabLine from Trigon-plus s.r.o.), a PCR cabinet from ESCO, a thermal bath from Memmert, and standard chemical equipment. In cooperation with the Faculty of Medicine, this cell lab enables us to maintain the studied mammal cells during our experiments. When I returned from my PostDoc stay, I had the excellent opportunity to be responsible for the AFM setup, combined with an inverted microscope, in the new Nanocharacterization lab of Prof. J. Valenta, Ph.D. Our setup comprises an AFM NanoWizard 3 from JPK (now Bruker). See the photograph in Fig. 12; its schema is in Fig. 13.

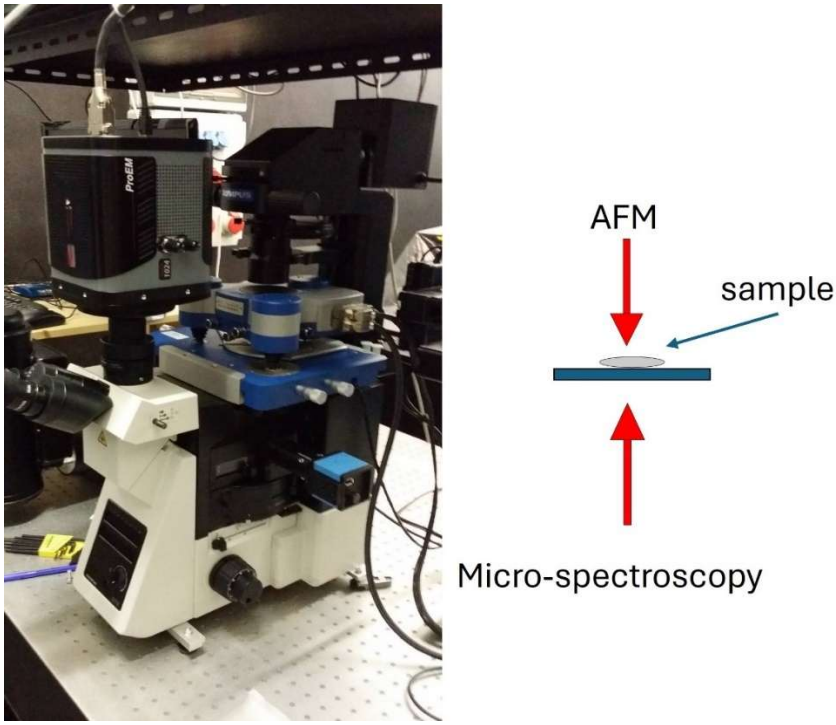

Figure 12: Photograph of the AFM setup integrated with a micro-spectroscopy setup. The AFM head is positioned on top of an inverted microscope, allowing the AFM to access the sample from above, while the micro-spectroscopy system accesses the sample from below through the sample support (e.g., mica, glass slide).

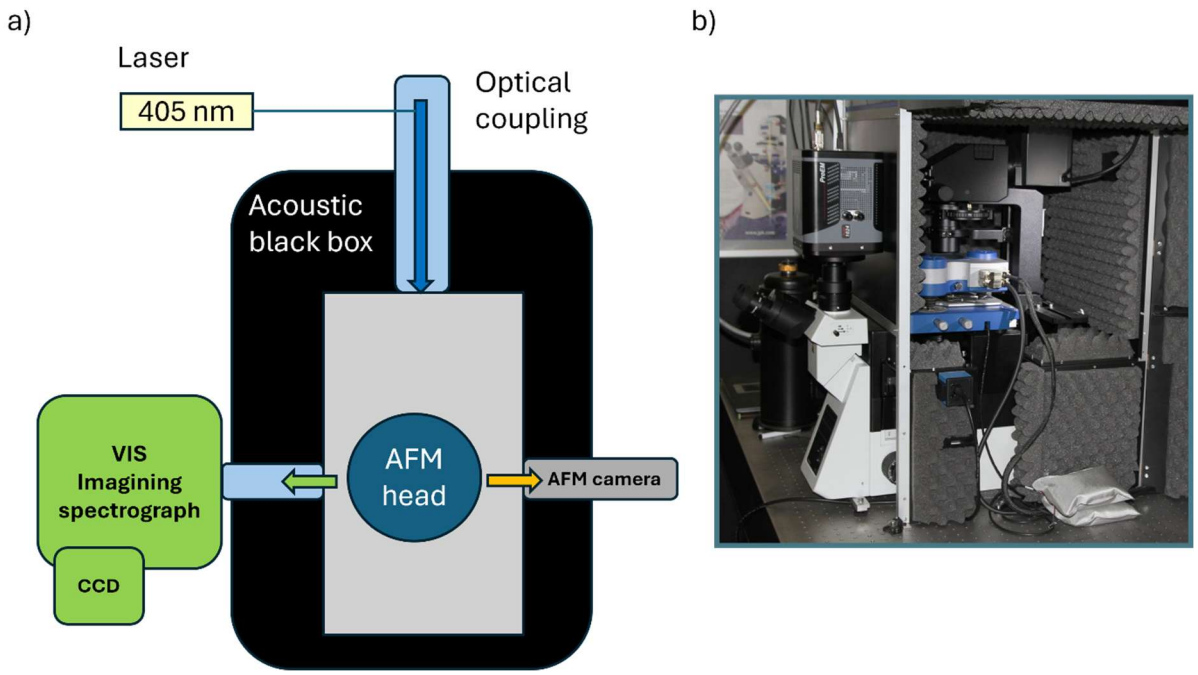

Figure 13: a) Scheme of the AFM setup with optical paths, b) AFM in the acoustic box.

As we can see in Fig. 12 and Fig. 13, the AFM head is placed on a manually controlled support table, which is placed on top of an inverted optical microscope Olympus IX-73. The sample supporting table has a central opening in the middle, allowing the objective a direct view of the AFM head /sample zone. This enables us to obtain and correlate an AFM image with the optical and spectroscopic image. The optical signal from the sample can be guided via three different pathways. The first pathway (orange arrow) leads the optical signal to the AFM camera (Imaginsource DFK31BF03); the second pathway leads to the top port of the microscope with microscope eyepieces (see image 13 b). This port is shared with another mount, which is adaptable to various cameras (including EM-CCD camera, PRoEM1024, and others). The last pathway (green arrow) guides the optical signal to the micro-spectroscopy setup consisting of a monochromator (Acton SpectraPro-2358i) and a nitrogen-cooled Princeton Instruments Spec-10:400 DDBI CCD camera.

The optical excitation of the sample is standardly performed via the back port of the microscope (blue arrow Fig. 13), where we have pathways of several mirrors leading the excitation from 405 nm (Swabian Instruments type 500, DL nSec SYNC rise and fall time < 2 ns) to the microscope. In the laboratory, other continuous lasers with emission wavelengths of 633 nm, 473 nm, and 375 nm, a white light source, and various LED diodes are available and can be coupled via the same pathway.

The sample is isolated from desk vibrations and placed on a sample holder supported by three magnetic mounts. The entire AFM system, including the microscope, is positioned on an anti-vibration table to prevent mechanical vibrations from the building from being transmitted to the AFM. Since we also work in acoustic measurement modes, the AFM and microscope can be enclosed in an acoustic box, as shown in Fig. 13 b). The complete setup, including the table, has

an acoustic resonance frequency of approximately 45–49 Hz. These frequencies should be avoided in the device's immediate vicinity during acoustic mode operation measurements.

The image alignment of all cameras and AFM was part of my student's, Pavel Doležal, Bc. Thesis [99]. There, he developed a protocol for finding maximal overlap between micro-spectroscopy and AFM images and calculated their magnification relations. Currently, for the silt width of 6μm, an area of 10-12 × 10-12 μm needs to be measured by the AFM to achieve 100% overlap between these two channels (the AFM and micro-spectroscopy). The AFM area needs to be slightly bigger than the slit due to the relatively big size of a pixel at a micro-spectroscopy setup and due to the unknown, precise position of the cantilever tip on the cantilever (uncertainty of 1-2 μm). In Fig. 14 a)-d) we can see the images of the cantilever on the Princeton CCD camera and its relation to the slit. In Fig. 14d, we can see the picture taken from the AFM camera, and in the inset, the measured AFM picture, we can see that the slit is oriented perpendicularly to the AFM camera. In Fig. 14, on the left side, we see the luminescent object as seen from the CCD camera, and on the right side, the same object measured by AFM.

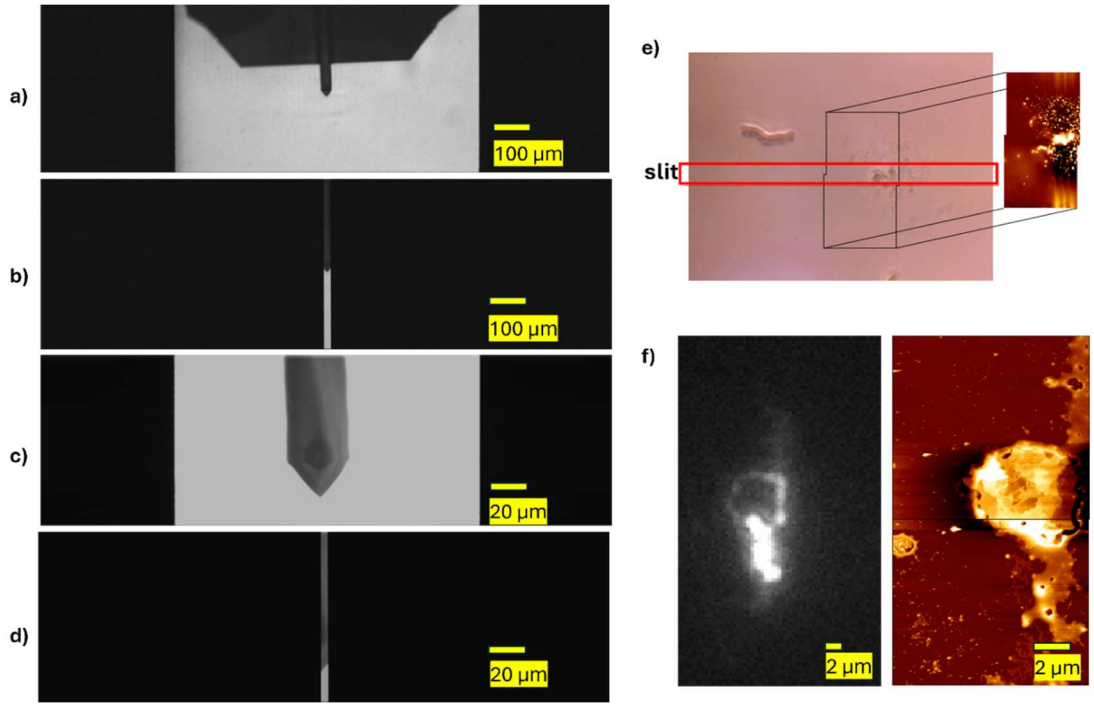

Figure 14: Image synchronization of AFM and micro-spectroscopy setup. a–b) Photographs of an ACTA cantilever captured using a 10× objective with the monochromator without the slit a) and with the slit b). c) The same cantilever imaged using a 60× objective without the slit c) and with the slit d), the slight width was 6 μm. e) Example of the sample area as seen through the AFM CCD camera, with the corresponding AFM image shown in the inset. The micro-spectroscopy slit is oriented perpendicularly to the AFM axis. (f) Example of a luminescent object imaged with the micro-spectroscopy setup (left) and the same object measured and visualized with AFM (right).

To be able to look simultaneously on the micro-spectroscopy camera, we needed to modify the AFM head by inserting a filter after the laser diode. We selected the filter (TechSpec 1000nm CWL, Hard Coated OD 4.0, 50nm Bandpass Filter), which sufficiently cuts all wavelengths below

around 935 nm. The filter was implemented in the AFM head by the JPK company. This had an unexpected result. Now, we have up to three times the signal from the laser reflection from the cantilever to the AFM detector, and at the same time, the noise is also significantly lower. This enables us to measure AFM data with better precision and detail and use cantilevers in harsher environments, such as biological solutions, which tend to oxidize the cantilever and diminish its reflectivity.

If necessary, the system can be connected via glass fibre to another microscope (Olympus IX-71) via an adapter and used with the another system cameras and detectors, which have spectral ranges VIS 370-1000 nm (spectrometer Action SpectraPro-2300i with a liquid nitrogen-cooled back-illuminated CCD camera (Princeton Instruments Spec-10:400B)) and NIR 950-1650 nm (Acton SpectraPro2500i with the InGaAs camera NIRvana, Princeton Instruments).

Our AFM setup has several extensions and various modules, including:

AFM QI advanced mode enables us to make point-by-point measurements of topological and mechanical properties of the samples. This mode will be upgraded by HQ Tapping mode during the year 2025, allowing us to measure faster and get a better mechanical properties map of the samples.

Akiyama probe module—This module serves as a tuning fork and enables us to obtain sample topography without using the feedback laser. This is crucial for simultaneous measurement of the AFM images and collecting luminescence spectra from the same spot without having strong scattering from the AFM laser. A prototype of this module was tested in our laboratory.

The scanning tunnelling microscopy (STM) module enables us to apply a bias Voltage of +/-10 V and measure in a current range of +/-100 nA to +/-10 nA with a gain of up to 100 V/μA. This enables us to measure down to single molecules/nanoparticles and obtain not only their conductivity but also, from the IV curve, we can obtain information about the NP band gap structure [100].

JPK Conductive module: This module requires a conductive tip and a conductive substrate. Generally, the tip is applied to the sample, and the current flow through the tip-sample contact is measured during AFM scanning. Although this module has less spatial resolution than the STM module, it can measure the samples with more complex topography.

JPK BioCell with Cell heater module: This module enables us to hold the temperature necessary for cell survival, so we can study the nanomechanical properties of cells in vitro. However, it does not supply the cells with CO_2, so the upper limit for cell observation is just a few hours.

The AFM can operate not only under dry conditions but also under liquid conditions. In case we would like to change the salinity of the liquid, change the pH, or add a controlled dose of nanoparticles or a drug, we can connect the **Microfluidics Chemyx Fusion 200**. This pump enables us to add down to 0.1-10 μl / min to the Petri dish in which we have submerged the sample during AFM measurement. In the future, we would like to connect this setup also to a Potentiostat (Metrohm Autolab PGSTAT302N 302), which would enable us to study electrochemistry on one particle with the AFM and ensemble within the same chemical conditions by the potentiostat.

4. Overview of the results

Overview of the results

As discussed in previous chapters, the physics and chemistry of nanoparticles, nanosurfaces, and their interactions with the biological environment are inherently complex. These systems must be studied using both ensemble (bulk) methods and high-resolution techniques. Yet, bulk methods often lack the precision and biological relevance required at the nanoscale. Therefore, single-particle analysis and surface characterization at nanometre resolution are essential, especially when addressing complex questions such as what parameters govern the formation of the protein corona on nanoparticles.

The studied nanoparticles were:

- Crystalline silicon nanoparticles with a thin organic shell, prepared from annealing of Hydrogen silsesquioxane [PI1], [PI2], [PI3].
- Crystalline P and B-doped silicon nanocrystals prepared by co-sputtering of Si, B_2O_3, and P_2O_5 into a Borophosphosilicate glass, which was further annealed, and then the doped nanoparticles were released by HF etching [PI4], [PI5].
- Silicon nanocrystals prepared from electrochemical etching, also known as porous silicon, from a B-doped wafer [PI6], [PI9].
- Nanodiamonds were supplied by NanoCarbon UDD-TAH, Diamond Centre, St. Petersburg, Russia. NDs were prepared by combustion of an oxygen-deficient explosive mixture of TNT/T4 in a closed chamber and afterwards purified in various acids [PI6]. Ultrasmall detonation nanodiamonds were used in the publication [PI8].
- Cerium nanoparticles were synthesised in a wet procedure from chemical precursors at low temperatures, and the resulting precipitates were purified from the synthesis solution [PI7].
- Silicon carbide nanoparticles were prepared using the wet chemical etching method of silicon carbide powder [PI10].
- Nanodroplets of poly-ε-caprolactone were electrosprayed on nanofibers, which were created by electrospraying and electrospinning of the same material [PI13].

The publications in this work can be divided into four categories based on the information and knowledge required to understand protein corona formation.

On the road to understanding the protein corona, it is essential to first understand nanoparticle synthesis. This allows us to gather detailed information about the conditions under which nanoparticles are prepared and to identify critical parameters that may vary between batches—variations that ensemble methods often fail to detect. We have referred to this group of publications as follows:

A) Nanoparticles from individualities to ensemble properties

This collection includes two publications [PI1], [PI2] [42], [101], and one patent [PI3] that address the problems of Si nanoparticle synthesis. Generally, the oxidized Si nanoparticles are biocompatible and biodegradable, but the emission from a single dot is too broad to be used as

a biological marker for single-object tracking. As seen from the literature[102] and the author's Ph.D. thesis publications, the emission of Si nanoparticles remains excessively broad.

If the Si nanoparticle is covered by organic ligands, then the optical properties, such as quantum yield, increase to values as high as 70%, but at the same time, these ligands are often not biocompatible, and the PL linewidth broadens even further [103]. Therefore, we were looking for alternative roads to synthesize Si nanoparticles that do not have these drawbacks. Since we did not have a proper Schlenk line and also a furnace with a temperature reaching 1200°C, we needed to synthesize Si nanoparticles in SiO_2 matrix from Hydrogen silsesquioxane (HSQ), following the standard procedures developed by Prof. J. Veinot [104]. I needed to improvise and developed a synthesis in which we heated an organosilanol matrix similar to HSQ, which I synthesized, and then annealed it at a temperature around 1000°C in a slightly reducing atmosphere (5% Hydrogen, 95% Argon). After this process, we obtained Si nanoparticles embedded in a one-layer Si-(C=O)-X ceramic shell in a residual SiO_2 matrix, which could be etched away in HF vapours. Identifying the correct chemical reactions leading to the formation of this shell proved challenging, as the quantity of produced Si nanoparticles was too low for SAXS and other analysis methods. Interestingly, the FTIR spectra of samples before and after annealing the synthesized HSQ matrix showed that certain organic molecules were preserved even after high-temperature annealing (see Fig. 15), which seemed quite unexpected. However, thanks to supporting experiments, I discovered that—depending on the complexity of the organosilicon structure—we could protect the entrapped organic molecules (such as methyl isobutyl ketone, MIBK) from burning at temperatures up to 1000 °C. To confirm this, I created 1D and 2D organosilanol matrices (where 1D refers to a planar structure, 2D to two perpendicular planes, and 3D to a cube). In the 1D planar matrix, the organic molecules decomposed at temperatures above 300 °C, whereas in the 2D matrix, they remained stable up to 600 °C. When entrapped in a 3D cage-like HSQ structure, the organic molecules were protected until the cage itself decomposed—around 1000 °C. At that point, we observed a sort of controlled combustion of the organic molecules in the furnace. However, since the oxygen required for CO_x formation originated solely from the HSQ-like matrix, once it was depleted, the remaining organic molecule bonded to the surface of the Si nanoparticle, creating a one-layer ceramic shell.

These Si NP with a thin shell exhibited ultranarrow emission band-widths. To reveal the principles behind the synthesis of these ultranarrow-emitting (full width at half maximum, FWHM, around 5 nm at room temperature) Si nanoparticles, we needed to employ both single-dot spectroscopy and macroscopic characterization, such as FTIR. In these synthesis experiments, we did not see variations between individual batches of Si nanoparticles when the same parameters were used. I found out that with the shell thickness variation, I also modify the FWHM of the Si nanoparticle. If a shorter carbon chain of the organic molecule was used during HSQ modification, it resulted in a narrower FWHM and a thinner shell, due presence of shorter molecules [PI2].

The narrow emission linewidth of these nanoparticles holds great potential for biological applications, particularly for single-object tracking. However, scaling up their production would require more time than was available during the postdoctoral stay. Therefore, we decided to patent the process, with the intention of selling the patent rights [PI3] and enabling mass production on an industrial scale.

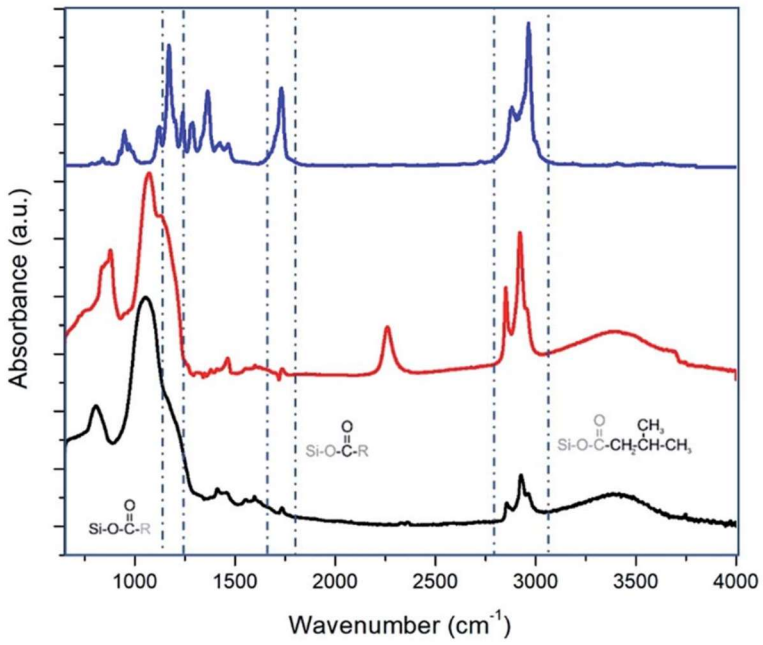

Figure 15: ATR-FTIR spectra of MIBK (blue line) non-annealed in-HSQ-MIBK (red line) and in HSQ-MIBK after thermal annealing (black line) on a silicon wafer (taken from [PI2]).

In the case of publication [PI4], the FWHM of a single boron and phosphorus-doped nanoparticle was down to 15 meV, but at 77 K and at room temperature, it was significantly higher.

The above-mentioned and other nanoparticles have been studied in the second group of publications. Here, I summarize our efforts to observe how the nanoparticles interact with the biological environment in the hope that we will reveal the principles behind their toxicity/biocompatibility and enable them to be used as biological markers.

B) Nanoparticles interacting with the biological environment

The same nanoparticles used in publication [PI4] were tested on human osteoblast cells in order to reveal their toxicity/biocompatibility; our results are summarized in publication [PI5]. We obtained several batches of phosphorus-boron-doped Si nanoparticles (Si-PB-NPs) manufactured in Prof. Minoru Fujii's laboratory in Japan. Their macroscopic characterization, including the FTIR, showed that the nanoparticles are the same in all the batches within the measurement error. Nevertheless, we discovered that one batch exhibited significantly higher toxicity than the others, even though all were delivered at the same time and prepared using the same procedure. After deep analysis, we discovered that the nanoparticles from the more cytotoxic batch were about a month fresher than the others. If we kept the Si-PB-NPs for a longer time in water (about 2 weeks), the cytotoxicity went to the same values as the other batches. We concluded that reactive oxygen species have been sterically hindered on the nanoparticle surface, which we could not detect by the ensemble measurements. Still, their presence significantly affected the biochemical interactions and, therefore, the biocompatibility of these nanoparticles. When we examined individual nanoparticles using single-dot spectroscopy and compared fresh and aged Si-PB-NPs, we observed a shift in the emission peak and changes in quantum efficiency, as summarized in [PI5]. Once again, a nanoscale investigation provided key insight into macroscale biological interactions.

As a further step in the protein corona formation study, I tried to gain insight into how a change in the nanoparticles' zeta potential affects the interaction with the biological environment by comparing two types of nanoparticles. As one sample, we selected our most used nanoparticles i.e. silicon nanocrystals, and as a comparison material, I chose nanodiamonds in order to observe how zeta-potential affects the interaction with the biological environment [PI6]. Si-NCs prepared by electrochemical etching have a negative zetapotential (around – 40 mV), whereas nanodiamonds (NDs) have a positive zetapotential (around +25 mV). What we found out is that in the nutrient medium, they have about the same zetapotential around zero due to non-specific formation of protein corona. However, they still behave differently and interact differently with the biological environment. The NDs have been shown to be more toxic after 48 hours of exposure to the cell, indicating that the toxicity might be caused by inflammation. When we looked at confocal microscopy and SEM, we found out that the NDs significantly affect the cell membrane and interact with the cytoskeleton, creating so-called blebs (confluent actin area without visible fibers). This agrees with finding that positively charged nanoparticles are more toxic, as proved, for example, by these articles [38] and [39]. In the case of silicon nanocrystals, we saw that they are perfectly biocompatible, and we even managed to observe spectra coming from a single silicon nanoparticle inside a living cell using our older micro-spectroscopy setup (see Fig. 16).

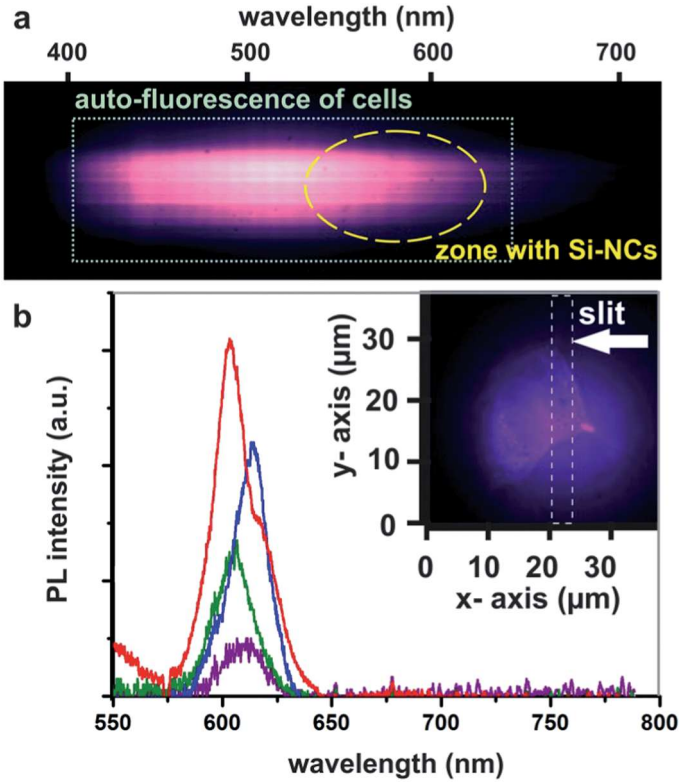

Figure 16: Micro-spectroscopy of Si-NCs in live SAOS-2 cells, (a) PL spectral image of the slit-defined area of the cell (b inset) fluorescence image of SAOS-2 cell (excitation 405 nm) with contours of the slit, defining the area from which PL spectra are taken. One can clearly see the broad cell-auto-fluorescence and also the spectral zone where the Si-NCs are emitting. (b) Emission spectra of several single Si-NCs upon subtracting the auto-fluorescence background (taken from [PI6]).

From the article [PI5], it was clear that silicon nanoparticles, which are not fully oxidised, can cause the formation of reactive oxygen species (ROS); therefore, we looked at the biological

interaction with Cerium nanoparticles, which are known as ROS scavengers [PI7]. When comparing differently passivated Cerium nanoparticles, we found out that the covering of Cerium nanoparticles has a significant influence on the nanoparticle behaviour in the cells. The poly(acrylic acid) covered cerium nanoparticles were found to be the most promising as a ROS scavenger, whereas dextryl covered nanoparticles and commercially available non-covered cerium nanoparticles showed mild to high toxicity. We also observed that the amount of absorbed protein mass is significantly different depending on the surface covering. These measurements gave us information about the mass of protein absorbed, but we did not gain any information about the protein corona formation and composition, not to mention protein orientation/deformation. As another step, we returned to nanodiamonds, namely 1-5 nm nanodiamonds with either oxygen or hydrogen termination. What was found by bioinformatics characterization of the identified proteins points to the strong influence of electrostatic interaction between proteins and NP, depending on their termination [PI8]. In this article, we approached the identification of proteins by means of mass characterization, which, in this case, was mass spectroscopy. Generally, the nanoparticles were incubated with biological material, then separated from non-bonded material by centrifugation, and then the protein corona was stripped down from the nanoparticles by trypsin[105]. Although we were able to find out what proteins have been present in the protein corona and that there is a difference in protein corona formation for oxygen and hydrogen nanodiamonds, with this approach, we could not study protein corona in the native state.

We intended to address the last two issues in order to obtain a more complete picture of how nanoparticles interact with the biological environment from a macroscale perspective: Do the same nanoparticles interact differently with different types of cells? [PI9], and what kind of immune response does the biological system exhibit? [PI10]. In the case of article [PI9], we studied phosphorus-boron-doped Si nanoparticles, which were studied for up to 48 hours in standard conditions in the presence of FBS and in nonstandard conditions, where the nanoparticles were incubated with the cells without FBS for the first 6 hours. These experiments demonstrated that when nanoparticles are incubated without FBS, protein corona formation is prevented, and the nanoparticles exhibit more toxic effects compared to conditions where the protein corona has time to form before interacting with cells. This trend was consistent across all tested cell types, suggesting that the protein corona may also have a protective role in mitigating nanoparticle toxicity. The alternations of surface termination also showed that the immunresponse is governed by the surface of the nanoparticle [PI10]. Even though different terminations of Si NPs do not have a significant effect on their colloidal stability in the cultivation media, they play a key role with respect to human cells. Monocytes, being a key part of the immune system, produce a variety of cytokines upon contact with these NPs and mark them as a potential immunomodulatory material [PI10]. From the biological experiments, it was clear that ensemble measurements cannot directly access the protein corona. Even slight variations of nanoparticle surface groups significantly impact protein corona formation and biological reactions; ensemble experiments cannot adequately access these variations. Also, in the case of interaction with living cells, we need to rely on statistics from a relatively small number of experiments. The biological experiments are also dependent on outside parameters such as batches of foetal bovine serum (FBS), which are different, since they are harvested from living organisms, which, of course, have not only different genetic material but also the composition varies depending on the animal's living conditions. It was also clear that we obtained different results if we covered the nanoparticles with a corona and then exposed them to living cells or incubated them without previous corona formation. These findings clearly indicate that to

properly understand protein corona formation, we must examine the process at the nanoscale and under in vivo-like conditions. One suitable tool for this is AFM, which can also operate in liquid environments. With a bit of luck, we started to collaborate with a group of Dmytro A. Yushchenko from UOCHAB, Czech Republic, who worked on the *α*-synuclein protein. We tried to visualize this protein and its formation; the gained knowledge is summarized in the next group of papers.

C) From single proteins to their ensembles

α-synuclein is naturally found in living organisms, and in its free form, it is harmless. However, once it starts to agglomerate and polymerize, it has a significant impact on the health of the affected living organism. Polymerization of this protein is observed in patients with Parkinson's disease. In a group of publications [PI11], [PI12], we explored the aggregation of neuronal protein *α*-synuclein and the formation of amyloid fibrils. We were also interested in how individual protein units are packed and folded under a change of experimental conditions. Although bulk or ensemble-based analytical methods can provide information about the total mass of fibrils formed, they cannot resolve the length or packing of individual proteins within these fibrils. Therefore, we developed a procedure that allowed us to observe fibrils and individual protein units under near-native conditions. The fibrils were deposited on freshly cleaved mica and studied within a two-hour window after preparation, while they were still wet. In publication [PI12] we explored how modification of C-terminal end of the fibril affect its further grow, the data indicate that incorporation of the monomeric *α*-synuclein in fibrils during their elongation stage is a process that has at least two steps, which, we assume, are the initial binding of the monomer to the fibril and the following adopting of amyloid conformation by the monomer [PI12]. In article [PI11], we explored the minimal material concentrations by which the fibril starts to form. The critical concentration of α-synuclein fibril growth is ~0.4 μM. Prefibrillar amyloid aggregates appear at concentrations between 0.45 and 3 μM and are an intermediate state between monomers and fibrils. Although morphologically different from fibrils, prefibrillar aggregates have similar properties to those of fibrils.

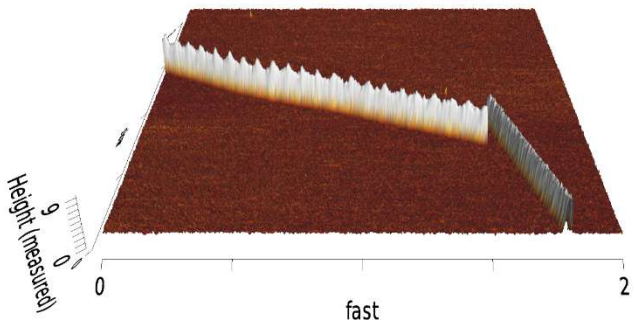

Figure 17: 3D AFM picture of α-synuclein.

The visualization of individual fibres was crucial in revealing the detailed structure and packing of proteins (see Fig. 17). In the final paper included in this thesis, I aimed to explore in greater detail what happens when a sample has a nanoscale surface modification and how this affects its interaction with cells.

D) How does nano surfacing affect the interaction with cells

Here, I would like to discuss just one paper in which we studied how a nanofibrous layer (scaffold) with nanodroplets interacts with the biological environment [PI13]. The intended use of this material is to prevent the ingrowth of individual tissue layers after the operation, since these ingrowths are painful and reoperation is needed. For example, during a caesarean section, up to nine layers of tissue are cut to reach the baby in the womb. After birth, these layers must be stitched together one by one, and during healing, ingrowth can occur in one or more of them. The developed scaffold is based on biocompatible and biodegradable poly-ε-caprolactone, and it serves as a spacer in the operation between two layers of tissue. The scaffold should be reabsorbed within a few months after the operation. My task there was to study various modifications of this scaffold in the biological relevant scale, in the scale of filopodia (20-100 nm). The AFM measurements were particularly challenging because the scaffold was thicker than the working Z-range of the AFM. We also measured individual fibers that overlapped in a structure resembling dress fabric. Under pressure, they behaved like rubber bands—if too much force was applied, they not only bent but also acted like a catapult, potentially damaging the AFM cantilever. Therefore, it was essential to carefully balance the applied force and scanning speed to obtain reliable results. The AFM data revealed that, at the biologically relevant scale, individual scaffold samples differed in their adhesion forces. These findings correlated with biological experiments and helped explain differences in cell behaviour that were not evident from bulk properties such as wettability, which appeared similar across samples.

This study, along with the others discussed above, provided a solid foundation for our ongoing investigation of protein corona formation at the nanoscale.

Appendix: Collection of publications

[PI1] I. Sychugov, A. Fucikova, F. Pevere, Z. Yang, J. G. C. Veinot, and J. Linnros, „Ultranarrow Luminescence Linewidth of Silicon Nanocrystals and Influence of Matrix", ACS PHOTONICS, 1, 10, 998–1005, 2014, doi: 10.1021/ph500221z.

[PI2] A. Fucikova, I. Sychugov, and J. Linnros, „The shell matters: one step synthesis of core–shell silicon nanoparticles with room temperature ultranarrow emission linewidth", Faraday Discuss., 222, 0, 135–148, 2020, doi: 10.1039/C9FD00093C.

[PI3] A. Fucikova, J. Linnros, and I. Sychugov, „Synthesized thin shell passivated silicon nanocrystals with a narrow photoluminescence linewidth", US10287494B2, granted 14. May 2019. https://patents.google.com/patent/US10287494B2/en

[PI4] T. Kanno, H. Sugimoto, A. Fucikova, J. Valenta, and M. Fujii, „Single-dot spectroscopy of boron and phosphorus codoped silicon quantum dots", J. Appl. Phys., 120, 16, 164307, 2016, doi: 10.1063/1.4965986.

[PI5] L. Ostrovska, A. Broz, A. Fucikova, A T. Belinova, H. Sugimoto, T. Kanno, M. Fujii, J. Valenta, M.H. Kalbacova, L. Ostrovska „The impact of doped silicon quantum dots on human osteoblasts", RSC Adv., 6, 68, 63403–63413, 2016, doi: 10.1039/C6RA14430F.

[PI6] A. Fucikova, J. Valenta, I. Pelant, M. Hubalek Kalbacova, A. Broz, B. Rezek, A. Kromka and Z. Bakaeva: „Silicon nanocrystals and nanodiamonds in live cells: photoluminescence characteristics, cytotoxicity and interaction with cell cytoskeleton", RSC Adv., 4, 20, 10334–10342, 2014, doi: 10.1039/C3RA47574C.

[PI7] X.H. Ju, A. Fucikova, B. Smid, J. Novakova, I. Matolinova, V. Matolin, M. Janata, T. Belinova, M.H. Kalbacova, „Colloidal stability and catalytic activity of cerium oxide nanoparticles in cell culture media", RSC Adv., 10, 65, 39373–39384, 2020, doi: 10.1039/D0RA08063B.

[PI8] I. Machova, M. Hubalek, T. Belinova, A. Fucikova, S. Stehlik, B. Rezek, M.Hubalek Kalbacova, „The bio-chemically selective interaction of hydrogenated and oxidized ultra-small nanodiamonds with proteins and cells", Carbon, 162, 650–661, 2020, doi: 10.1016/j.carbon.2020.02.061.

[PI9] T. Belinova, L. Vrabcova, I. Machova, A. Fucikova, J. Valenta, H. Sugimoto, M. Fujii, M. Hubalek Kalbacova, „Silicon Quantum Dots and Their Impact on Different Human Cells", Phys. Status Solidi B, 255, 10, 1700597, 2018, doi: https://doi.org/10.1002/pssb.201700597.

[PI10] T. Belinova, I. Machova, D. Beke, A. Fucikova, A. Gali, Z. Humlova, J. Valenta, M. Hubalek Kalbacova „Immunomodulatory Potential of Differently-Terminated Ultra-Small Silicon Carbide Nanoparticles", Nanomaterials, 10, 3, 2020, doi: 10.3390/nano10030573.

[P11] K. Afitska, A. Fucikova, V. V. Shvadchak, a D. A. Yushchenko, „α-Synuclein aggregation at low concentrations", Biochim. Biophys. Acta BBA - Proteins Proteomics, 1867, 7, 701–709, 2019, doi: 10.1016/j.bbapap.2019.05.003.

[P12] K. Afitska, A. Fucikova, V. V. Shvadchak, a D. A. Yushchenko, „Modification of C Terminus Provides New Insights into the Mechanism of α-Synuclein Aggregation", Biophys. J., roč. 113, č. 10, s. 2182–2191, lis. 2017, doi: 10.1016/j.bpj.2017.08.027.

[PI13] M. Klicova, Z. Oulehlova, A. Klapstova, M. Hejda, M. Krejcik, O. Novak, J. Mullerova, J. Erben, J. Rosendorf, R. Palek, V. Liska, A. Fucikova, J. Chvojka, I. Zvercova, J. Horakova, „Biomimetic hierarchical nanofibrous surfaces inspired by superhydrophobic lotus leaf structure for preventing tissue adhesions", Mater. Des., 217, 110661, 2022, doi: 10.1016/j.matdes.2022.110661.

5. Conclusion and outlook

The research presented in this thesis focused on different aspects of studying interactions between nanomaterials, especially nanoparticles, and the biological environment. These interactions depend not only on the composition of the nanomaterials but also on their shape, surface charge, and, most importantly, the protein corona that forms when nanomaterials are exposed to biological surroundings.

From papers in collection A, we can see that we need to look at and characterize individual nanoparticles in order to explain the behaviour of the ensemble. Ensemble-based methods are not precise enough, for example, to identify variance between individual batches of samples, which can have a serious impact on their cytotoxicity, as addressed in collection B. The nanoparticle cytotoxicity has many origins, one of which is somewhat expected: they are made from toxic elements. Another originates from their needle-like morphology, but also a surface charge, especially a positive one, has a negative effect on cell viability. Last but not least, the key determining the destiny of the nanoparticle in the cell is the protein corona, because the cell recognizes the protein corona first, and only later, the core, including the nanoparticle, might be exposed to the intracellular environment. As demonstrated in our papers, bulk methods reveal little about the native structure of the protein corona beyond its composition. Therefore, in Collection C, we investigated individual protein units, and in Collection D, we explored how nanostructured surfaces affect interactions with cells. The primary method we used to study nanoparticle-cell interactions and protein corona formation was Atomic Force Microscopy (AFM). In Chapter 2, we explore the principles behind the individual capabilities of AFM and compare them to their macro-/ensemble-based counterparts. Chapter 3 details our experimental setup, and Chapter 4 summarizes the results we obtained.

Now, I am working on the direct study of protein corona formation in vivo conditions. I developed an anchoring system with the help of my students, where a nanoparticle is bound to the surface for just about 15%, and we are looking for individual proteins that are coming to the anchored nanoparticle. These experiments will give us information not only on how many proteins are bound to a nanoparticle but also how stable they are, if they are deforming, etc. Our main goal is to reveal how fast the protein corona forms, how rigid it is, and how it affects the properties of the cell membrane upon entering the cell. Our approach—single-dot characterization—offers a new perspective on this topic, which is still predominantly explored using ensemble-based methods that often overlook the subtle but critical differences in individual NP properties within a population. Modulation of NP properties will show which NP feature has the most significant influence on the cell membrane upon NP entry and reveal sources of secondary toxicity of NPs.

6. List of abbreviations:

AFM	atomic force microscopy/microscope
DMA	Dynamic Mechanical Analysis
EE	electrochemically etched
FBS	foetal bovine serum
FTIR	Fourier transform infrared spectroscopy
FWHM	Full width at half maximum
HSQ	Hydrogen silsesquioxane
MIBK	Methyl isobutyl ketone
ND	nanodiamonds
NP	nanoparticle
PL	photoluminescence
ROS	reactive oxygen species
Si-NCs	silicon nanocrystals (prepared by electrochemical etching)
Si-PB-NPs	Phosphorus-boron-doped Si nanoparticles
SEM	Scanning electron microscopy
STM	scanning tunnelling microscopy

7. References

[1] I. Khan, K. Saeed, and I. Khan, 'Nanoparticles: Properties, applications and toxicities', *Arab. J. Chem.*, vol. 12, no. 7, pp. 908–931, Nov. 2019, doi: 10.1016/j.arabjc.2017.05.011.

[2] Q. Wu *et al.*, 'Formation and detection of biocoronas in the food industry and their fate in the human body', *Food Res. Int.*, vol. 174, p. 113566, Dec. 2023, doi: 10.1016/j.foodres.2023.113566.

[3] N. Joudeh and D. Linke, 'Nanoparticle classification, physicochemical properties, characterization, and applications: a comprehensive review for biologists', *J. Nanobiotechnology*, vol. 20, no. 1, p. 262, June 2022, doi: 10.1186/s12951-022-01477-8.

[4] J. Valenta *et al.*, 'Light-Emission Performance of Silicon Nanocrystals Deduced from Single Quantum Dot Spectroscopy', *Adv. Funct. Mater.*, vol. 18, no. 18, pp. 2666–2672, 2008, doi: https://doi.org/10.1002/adfm.200800397.

[5] L. Ostrovska *et al.*, 'The impact of doped silicon quantum dots on human osteoblasts', *RSC Adv.*, vol. 6, no. 68, pp. 63403–63413, July 2016, doi: 10.1039/C6RA14430F.

[6] 'Size-Dependent In Vivo Transport of Nanoparticles: Implications for Delivery, Targeting, and Clearance | ACS Nano'. Accessed: Apr. 16, 2024. [Online]. Available: https://pubs.acs.org/doi/10.1021/acsnano.3c05853

[7] V. De Matteis, 'Exposure to Inorganic Nanoparticles: Routes of Entry, Immune Response, Biodistribution and In Vitro/In Vivo Toxicity Evaluation', *Toxics*, vol. 5, no. 4, p. 29, Oct. 2017, doi: 10.3390/toxics5040029.

[8] T. Wu and M. Tang, 'Review of the effects of manufactured nanoparticles on mammalian target organs', *J. Appl. Toxicol.*, vol. 38, no. 1, pp. 25–40, 2018, doi: 10.1002/jat.3499.

[9] A. Kermanizadeh, D. Balharry, H. Wallin, S. Loft, and P. Møller, 'Nanomaterial translocation–the biokinetics, tissue accumulation, toxicity and fate of materials in secondary organs–a review', *Crit. Rev. Toxicol.*, vol. 45, no. 10, pp. 837–872, Nov. 2015, doi: 10.3109/10408444.2015.1058747.

[10] Z. Azim *et al.*, 'A review summarizing uptake, translocation and accumulation of nanoparticles within the plants: current status and future prospectus', *J. Plant Biochem. Biotechnol.*, vol. 32, no. 2, pp. 211–224, June 2023, doi: 10.1007/s13562-022-00800-6.

[11] V. Rajput *et al.*, 'Accumulation of nanoparticles in the soil-plant systems and their effects on human health', *Ann. Agric. Sci.*, vol. 65, no. 2, pp. 137–143, Dec. 2020, doi: 10.1016/j.aoas.2020.08.001.

[12] A. Sukhanova, S. Bozrova, P. Sokolov, M. Berestovoy, A. Karaulov, and I. Nabiev, 'Dependence of Nanoparticle Toxicity on Their Physical and Chemical Properties', *Nanoscale Res. Lett.*, vol. 13, no. 1, p. 44, Feb. 2018, doi: 10.1186/s11671-018-2457-x.

[13] M. Bundschuh *et al.*, 'Nanoparticles in the environment: where do we come from, where do we go to?', *Environ. Sci. Eur.*, vol. 30, no. 1, p. 6, 2018, doi: 10.1186/s12302-018-0132-6.

[14] A. Jain, S. Ranjan, N. Dasgupta, and C. Ramalingam, 'Nanomaterials in food and agriculture: An overview on their safety concerns and regulatory issues', *Crit. Rev. Food Sci. Nutr.*, vol. 58, no. 2, pp. 297–317, Jan. 2018, doi: 10.1080/10408398.2016.1160363.

[15] R. Abbasi, G. Shineh, M. Mobaraki, S. Doughty, and L. Tayebi, 'Structural parameters of nanoparticles affecting their toxicity for biomedical applications: a review', *J. Nanoparticle Res.*, vol. 25, no. 3, p. 43, Feb. 2023, doi: 10.1007/s11051-023-05690-w.

[16] J. R. Bathi, L. Wright, and E. Khan, 'Critical Review of Engineered Nanoparticles: Environmental Concentrations and Toxicity', *Curr. Pollut. Rep.*, vol. 8, no. 4, pp. 498–518, Dec. 2022, doi: 10.1007/s40726-022-00237-4.

[17] W. Qamar *et al.*, 'An insight into impact of nanomaterials toxicity on human health', *PeerJ*, vol. 12, p. e17807, Sept. 2024, doi: 10.7717/peerj.17807.

[18] C. Buzea, I. I. Pacheco, and K. Robbie, 'Nanomaterials and nanoparticles: sources and toxicity', *Biointerphases*, vol. 2, no. 4, pp. MR17-71, Dec. 2007, doi: 10.1116/1.2815690.
[19] J. B. Raftis and M. R. Miller, 'Nanoparticle translocation and multi-organ toxicity: A particularly small problem', *Nano Today*, vol. 26, pp. 8–12, June 2019, doi: 10.1016/j.nantod.2019.03.010.
[20] C. Chang, 'The immune effects of naturally occurring and synthetic nanoparticles', *J. Autoimmun.*, vol. 34, no. 3, pp. J234–J246, May 2010, doi: 10.1016/j.jaut.2009.11.009.
[21] G. Fotakis and J. A. Timbrell, 'In vitro cytotoxicity assays: comparison of LDH, neutral red, MTT and protein assay in hepatoma cell lines following exposure to cadmium chloride', *Toxicol. Lett.*, vol. 160, no. 2, pp. 171–177, Jan. 2006, doi: 10.1016/j.toxlet.2005.07.001.
[22] B. Kong, J. H. Seog, L. M. Graham, and S. B. Lee, 'Experimental considerations on the cytotoxicity of nanoparticles', *Nanomed.*, vol. 6, no. 5, pp. 929–941, July 2011, doi: 10.2217/nnm.11.77.
[23] A. B. Djurišić *et al.*, 'Toxicity of metal oxide nanoparticles: mechanisms, characterization, and avoiding experimental artefacts', *Small Weinh. Bergstr. Ger.*, vol. 11, no. 1, pp. 26–44, Jan. 2015, doi: 10.1002/smll.201303947.
[24] J. M. Wörle-Knirsch, K. Pulskamp, and H. F. Krug, 'Oops they did it again! Carbon nanotubes hoax scientists in viability assays', *Nano Lett.*, vol. 6, no. 6, pp. 1261–1268, June 2006, doi: 10.1021/nl060177c.
[25] H. Bahadar, F. Maqbool, K. Niaz, and M. Abdollahi, 'Toxicity of Nanoparticles and an Overview of Current Experimental Models', *Iran. Biomed. J.*, vol. 20, no. 1, pp. 1–11, Jan. 2016, doi: 10.7508/ibj.2016.01.001.
[26] H. L. Karlsson, S. Di Bucchianico, A. R. Collins, and M. Dusinska, 'Can the comet assay be used reliably to detect nanoparticle-induced genotoxicity?', *Environ. Mol. Mutagen.*, vol. 56, no. 2, pp. 82–96, Mar. 2015, doi: 10.1002/em.21933.
[27] H. I. Labouta *et al.*, 'Understanding and improving assays for cytotoxicity of nanoparticles: what really matters?', *RSC Adv.*, vol. 8, no. 41, pp. 23027–23039, 2018, doi: 10.1039/C8RA03849J.
[28] Z. Xiu, Q. Zhang, H. L. Puppala, V. L. Colvin, and P. J. J. Alvarez, 'Negligible Particle-Specific Antibacterial Activity of Silver Nanoparticles', *Nano Lett.*, vol. 12, no. 8, pp. 4271–4275, Aug. 2012, doi: 10.1021/nl301934w.
[29] A. Nel, T. Xia, L. Mädler, and N. Li, 'Toxic potential of materials at the nanolevel', *Science*, vol. 311, no. 5761, pp. 622–627, Feb. 2006, doi: 10.1126/science.1114397.
[30] D. Docter, D. Westmeier, M. Markiewicz, S. Stolte, S. K. Knauer, and R. H. Stauber, 'The nanoparticle biomolecule corona: lessons learned – challenge accepted?', *Chem. Soc. Rev.*, vol. 44, no. 17, pp. 6094–6121, Aug. 2015, doi: 10.1039/C5CS00217F.
[31] C. Corbo, R. Molinaro, A. Parodi, N. E. Toledano Furman, F. Salvatore, and E. Tasciotti, 'The impact of nanoparticle protein corona on cytotoxicity, immunotoxicity and target drug delivery', *Nanomed.*, vol. 11, no. 1, pp. 81–100, Jan. 2016, doi: 10.2217/nnm.15.188.
[32] R. Cai and C. Chen, 'The Crown and the Scepter: Roles of the Protein Corona in Nanomedicine', *Adv. Mater.*, vol. 31, no. 45, p. 1805740, 2019, doi: https://doi.org/10.1002/adma.201805740.
[33] S. J. Park, 'Protein-Nanoparticle Interaction: Corona Formation and Conformational Changes in Proteins on Nanoparticles', *Int. J. Nanomedicine*, vol. 15, pp. 5783–5802, 2020, doi: 10.2147/IJN.S254808.
[34] T. Bělinová *et al.*, 'Immunomodulatory Potential of Differently-Terminated Ultra-Small Silicon Carbide Nanoparticles', *Nanomaterials*, vol. 10, no. 3, Mar. 2020, doi: 10.3390/nano10030573.
[35] I. Machova *et al.*, 'The bio-chemically selective interaction of hydrogenated and oxidized ultra-small nanodiamonds with proteins and cells', *Carbon*, vol. 162, pp. 650–661, June 2020, doi: 10.1016/j.carbon.2020.02.061.

[36] S. Tenzer *et al.*, 'Rapid formation of plasma protein corona critically affects nanoparticle pathophysiology', *Nat. Nanotechnol.*, vol. 8, no. 10, Art. no. 10, Oct. 2013, doi: 10.1038/nnano.2013.181.
[37] A. Panas *et al.*, 'Screening of different metal oxide nanoparticles reveals selective toxicity and inflammatory potential of silica nanoparticles in lung epithelial cells and macrophages', *Nanotoxicology*, vol. 7, no. 3, pp. 259–273, May 2013, doi: 10.3109/17435390.2011.652206.
[38] W.-S. Cho *et al.*, 'Zeta Potential and Solubility to Toxic Ions as Mechanisms of Lung Inflammation Caused by Metal/Metal Oxide Nanoparticles', *Toxicol. Sci.*, vol. 126, no. 2, pp. 469–477, Apr. 2012, doi: 10.1093/toxsci/kfs006.
[39] X. Shao *et al.*, 'Independent effect of polymeric nanoparticle zeta potential/surface charge, on their cytotoxicity and affinity to cells', *Cell Prolif.*, vol. 48, no. 4, pp. 465–474, May 2015, doi: 10.1111/cpr.12192.
[40] F. Bertoli, D. Garry, M. P. Monopoli, A. Salvati, and K. A. Dawson, 'The Intracellular Destiny of the Protein Corona: A Study on its Cellular Internalization and Evolution', *ACS Nano*, vol. 10, no. 11, pp. 10471–10479, Nov. 2016, doi: 10.1021/acsnano.6b06411.
[41] 'Ultranarrow Luminescence Linewidth of Silicon Nanocrystals and Influence of Matrix | ACS Photonics'. Accessed: Feb. 03, 2021. [Online]. Available: https://pubs.acs.org/doi/10.1021/ph500221z
[42] A. Fucikova, I. Sychugov, and J. Linnros, 'The shell matters: one step synthesis of core–shell silicon nanoparticles with room temperature ultranarrow emission linewidth', *Faraday Discuss.*, vol. 222, no. 0, pp. 135–148, June 2020, doi: 10.1039/C9FD00093C.
[43] A. Fucikova, J. Linnros, and I. Sychugov, 'Synthesized thin shell passivated silicon nanocrystals with a narrow photoluminescence linewidth', US10287494B2, May 14, 2019 Accessed: Feb. 03, 2021. [Online]. Available: https://patents.google.com/patent/US10287494B2/en
[44] A. Fucikova, I. Sychugov, and J. Linnros, 'Method for direct synthesis of silicon nanocrystals and a material comprising silicon nanocrystals having a core and a thin shell', SE543119C2, Oct. 06, 2020 Accessed: Apr. 22, 2024. [Online]. Available: https://patents.google.com/patent/SE543119C2/en?q=(anna+fucikova)&oq=anna+fucikova
[45] G. Binnig, C. F. Quate, and Ch. Gerber, 'Atomic Force Microscope', *Phys. Rev. Lett.*, vol. 56, no. 9, pp. 930–933, Mar. 1986, doi: 10.1103/PhysRevLett.56.930.
[46] B. Voigtländer, *Atomic Force Microscopy*. in NanoScience and Technology. Cham: Springer International Publishing, 2019. doi: 10.1007/978-3-030-13654-3.
[47] N. C. Santos and F. A. Carvalho, Eds, *Atomic Force Microscopy: Methods and Protocols*, vol. 1886. in Methods in Molecular Biology, vol. 1886. New York, NY: Springer, 2019. doi: 10.1007/978-1-4939-8894-5.
[48] J. M. Wallace, 'Applications of atomic force microscopy for the assessment of nanoscale morphological and mechanical properties of bone', *Bone*, vol. 50, no. 1, pp. 420–427, Jan. 2012, doi: 10.1016/j.bone.2011.11.008.
[49] S. V. Kontomaris, A. Stylianou, G. Chliveros, and A. Malamou, 'Overcoming Challenges and Limitations Regarding the Atomic Force Microscopy Imaging and Mechanical Characterization of Nanofibers', *Fibers*, vol. 11, no. 10, Art. no. 10, Oct. 2023, doi: 10.3390/fib11100083.
[50] P.-Y. Collart-Dutilleul *et al.*, 'Initial stem cell adhesion on porous silicon surface: molecular architecture of actin cytoskeleton and filopodial growth', *Nanoscale Res. Lett.*, vol. 9, no. 1, p. 564, Oct. 2014, doi: 10.1186/1556-276X-9-564.
[51] 'AFMworkshop'. [Online]. Available: https://www.afmworkshop.com/images/news2019/01/Measuring-and-understanding-force-distance-curves-v2.pdf

[52] M. Bartošík *et al.*, 'Nanometer-Sized Water Bridge and Pull-Off Force in AFM at Different Relative Humidities: Reproducibility Measurement and Model Based on Surface Tension Change', *J. Phys. Chem. B*, vol. 121, no. 3, pp. 610–619, Jan. 2017, doi: 10.1021/acs.jpcb.6b11108.
[53] J. E. Sader *et al.*, 'Spring constant calibration of atomic force microscope cantilevers of arbitrary shape', *Rev. Sci. Instrum.*, vol. 83, no. 10, p. 103705, Oct. 2012, doi: 10.1063/1.4757398.
[54] T. Hofrichterová, 'Mechanické vlastnosti hydrogelů - srovnání měření modulu pružnosti pomocí DMA a AFM Mechanical Properties of Hydrogels - Comparison between DMA and AFM Measurements of Elastic Modulus'. Matematicko-fyzikální fakulta, Univerzita Karlova, 2019. [Online]. Available: https://dspace.cuni.cz/handle/20.500.11956/108204
[55] S. V. Kontomaris, A. Malamou, and A. Stylianou, 'The Hertzian theory in AFM nanoindentation experiments regarding biological samples: Overcoming limitations in data processing', *Micron*, vol. 155, p. 103228, Apr. 2022, doi: 10.1016/j.micron.2022.103228.
[56] 'Bone Biology and Mechanics Lab: BBML'. Accessed: May 30, 2024. [Online]. Available: https://bbml.et.iupui.edu/afmintro.html
[57] 'Force measurements with the atomic force microscope: Technique, interpretation and applications - ScienceDirect'. Accessed: June 19, 2024. [Online]. Available: https://www.sciencedirect.com/science/article/pii/S0167572905000488
[58] A. Vinckier and G. Semenza, 'Measuring elasticity of biological materials by atomic force microscopy', *FEBS Lett.*, vol. 430, no. 1, pp. 12–16, June 1998, doi: 10.1016/S0014-5793(98)00592-4.
[59] S. V. Kontomaris, A. Stylianou, A. Georgakopoulos, and A. Malamou, 'Is it mathematically correct to fit AFM data (obtained on biological materials) to equations arising from Hertzian mechanics?', *Micron*, vol. 164, p. 103384, Jan. 2023, doi: 10.1016/j.micron.2022.103384.
[60] S. W. Chen, J.-M. Teulon, H. Kaur, C. Godon, and J.-L. Pellequer, 'Nano-structural stiffness measure for soft biomaterials of heterogeneous elasticity', *Nanoscale Horiz.*, vol. 8, no. 1, pp. 75–82, Dec. 2022, doi: 10.1039/D2NH00390B.
[61] E. Minelli *et al.*, 'A fully-automated neural network analysis of AFM force-distance curves for cancer tissue diagnosis', *Appl. Phys. Lett.*, vol. 111, no. 14, p. 143701, Oct. 2017, doi: 10.1063/1.4996300.
[62] J. R. Waite, S. Y. Tan, H. Saha, S. Sarkar, and A. Sarkar, 'Few-shot deep learning for AFM force curve characterization of single-molecule interactions', *Patterns*, vol. 4, no. 1, p. 100672, Jan. 2023, doi: 10.1016/j.patter.2022.100672.
[63] 'Machine learning assisted multifrequency AFM: Force model prediction | Applied Physics Letters | AIP Publishing'. Accessed: May 03, 2025. [Online]. Available: https://pubs.aip.org/aip/apl/article/123/23/231603/2926400/Machine-learning-assisted-multifrequency-AFM-Force
[64] 'Cellular Analysis by Atomic Force Microscopy', Routledge & CRC Press. Accessed: Mar. 17, 2025. [Online]. Available: https://www.routledge.com/Cellular-Analysis-by-Atomic-Force-Microscopy/Lekka/p/book/9789814669672
[65] I. Zlotnikov, E. Zolotoyabko, and P. Fratzl, 'Nano-scale modulus mapping of biological composite materials: Theory and practice', *Prog. Mater. Sci.*, vol. 87, pp. 292–320, June 2017, doi: 10.1016/j.pmatsci.2017.03.002.
[66] 'Hysitron Nanoindenters'. Accessed: May 04, 2025. [Online]. Available: https://www.bruker.com/en/products-and-solutions/test-and-measurement/nanomechanical-test-systems/hysitron-nanoindenters.html

[67] C.-K. Lee, Y.-M. Wang, L.-S. Huang, and S. Lin, 'Atomic force microscopy: Determination of unbinding force, off rate and energy barrier for protein–ligand interaction', *Micron*, vol. 38, no. 5, pp. 446–461, July 2007, doi: 10.1016/j.micron.2006.06.014.
[68] H. Sun, Z. Guo, H. Hong, P. Yu, Z. Xue, and H. Chen, 'Protein folding mechanism revealed by single-molecule force spectroscopy experiments', *Biophys. Rep.*, vol. 7, no. 5, pp. 399–412, Oct. 2021, doi: 10.52601/bpr.2021.210024.
[69] R. Lacombe, *Adhesion Measurement Methods: Theory and Practice*. Boca Raton: CRC Press, 2005. doi: 10.1201/9781420028829.
[70] R. Lacombe, *Adhesion Measurement Methods: Theory and Practice*. Boca Raton: CRC Press, 2005. doi: 10.1201/9781420028829.
[71] S. Sadegh Hassani, M. Daraee, and Z. Sobat, 'Application of atomic force microscopy in adhesion force measurements', *J. Adhes. Sci. Technol.*, vol. 35, no. 3, pp. 221–241, Feb. 2021, doi: 10.1080/01694243.2020.1798647.
[72] B. Cappella and G. Dietler, 'Force-distance curves by atomic force microscopy', *Surf. Sci. Rep.*, vol. 34, no. 1, pp. 1–104, Jan. 1999, doi: 10.1016/S0167-5729(99)00003-5.
[73] 'Scaling Effects on Materials Tribology: From Macro to Micro Scale'. Accessed: July 18, 2025. [Online]. Available: https://www.mdpi.com/1996-1944/10/5/550
[74] T. Ahmed, 'Chapter 4 - Fundamentals of Rock Properties', in *Reservoir Engineering Handbook (Fifth Edition)*, T. Ahmed, Ed., Gulf Professional Publishing, 2019, pp. 167–281. doi: 10.1016/B978-0-12-813649-2.00004-9.
[75] R. N. Wenzel, 'RESISTANCE OF SOLID SURFACES TO WETTING BY WATER', *Ind. Eng. Chem.*, vol. 28, no. 8, pp. 988–994, Aug. 1936, doi: 10.1021/ie50320a024.
[76] G. Wolansky and A. Marmur, 'Apparent contact angles on rough surfaces: the Wenzel equation revisited', *Colloids Surf. Physicochem. Eng. Asp.*, vol. 156, no. 1, pp. 381–388, Oct. 1999, doi: 10.1016/S0927-7757(99)00098-9.
[77] 'Contact Angle Measurements and Wettability | Nanoscience Instruments'. Accessed: July 04, 2024. [Online]. Available: https://www.nanoscience.com/techniques/tensiometry/contact-angle-measurements-and-wettability/
[78] J. T. Korhonen, T. Huhtamäki, O. Ikkala, and R. H. A. Ras, 'Reliable Measurement of the Receding Contact Angle', *Langmuir*, vol. 29, no. 12, pp. 3858–3863, Mar. 2013, doi: 10.1021/la400009m.
[79] S.-Y. Zhang and J.-G. Guo, 'Superhydrophobicity and compressive stability of *Salvinia* surface: Mechanical analysis and structural design', *Appl. Surf. Sci.*, vol. 627, p. 157274, Aug. 2023, doi: 10.1016/j.apsusc.2023.157274.
[80] 'Tunable Anisotropic Wettability of Rice Leaf-Like Wavy Surfaces - Lee - 2013 - Advanced Functional Materials - Wiley Online Library'. Accessed: June 05, 2024. [Online]. Available: https://onlinelibrary.wiley.com/doi/10.1002/adfm.201201541
[81] E. De Ranieri, 'Biological nanostructures: Transparent randomness', *Nat. Nanotechnol.*, pp. 1–1, June 2015, doi: 10.1038/nnano.2015.122.
[82] T. B. H. Schroeder, J. Houghtaling, B. D. Wilts, and M. Mayer, 'It's Not a Bug, It's a Feature: Functional Materials in Insects', *Adv. Mater.*, vol. 30, no. 19, p. 1705322, 2018, doi: 10.1002/adma.201705322.
[83] 'Microscopic pillars on insect wings give bugs an antibacterial superpower'. Accessed: July 18, 2025. [Online]. Available: https://www.science.org/content/article/microscopic-pillars-insect-wings-give-bugs-antibacterial-superpower
[84] J. Jenkins *et al.*, 'Antibacterial effects of nanopillar surfaces are mediated by cell impedance, penetration and induction of oxidative stress', *Nat. Commun.*, vol. 11, no. 1, p. 1626, Apr. 2020, doi: 10.1038/s41467-020-15471-x.

[85] G. D. Bixler and B. Bhushan, 'Bioinspired rice leaf and butterfly wing surface structures combining shark skin and lotus effects', *Soft Matter*, vol. 8, no. 44, pp. 11271–11284, Oct. 2012, doi: 10.1039/C2SM26655E.
[86] T. Sun, L. Feng, X. Gao, and L. Jiang, 'Bioinspired Surfaces with Special Wettability', *Acc. Chem. Res.*, vol. 38, no. 8, pp. 644–652, Aug. 2005, doi: 10.1021/ar040224c.
[87] O. Tricinci, T. Terencio, B. Mazzolai, N. M. Pugno, F. Greco, and V. Mattoli, '3D Micropatterned Surface Inspired by Salvinia molesta via Direct Laser Lithography', *ACS Appl. Mater. Interfaces*, vol. 7, no. 46, pp. 25560–25567, Nov. 2015, doi: 10.1021/acsami.5b07722.
[88] Matěj Černý, 'Replication of natural structured surfaces into polymer matrix'. UCT Prague, June 03, 2019. [Online]. Available: https://repozitar.vscht.cz/theses/29408
[89] H. J. Ensikat, P. Ditsche-Kuru, C. Neinhuis, and W. Barthlott, 'Superhydrophobicity in perfection: the outstanding properties of the lotus leaf', *Beilstein J. Nanotechnol.*, vol. 2, pp. 152–161, Mar. 2011, doi: 10.3762/bjnano.2.19.
[90] 'Following the Natures Lead: Lotus Effect Self-Cleaning', Nanografi Nano Technology. Accessed: June 03, 2024. [Online]. Available: https://nanografi.com/blog/following-the-natures-lead-lotus-effect-selfcleaning/
[91] L. Michalikova, B. Rezek, A. Kromka, and M. Kalbacova, 'CVD diamond films with hydrophilic micro-patterns for self-organisation of human osteoblasts', *Vacuum*, vol. 84, no. 1, pp. 61–64, Aug. 2009, doi: 10.1016/j.vacuum.2009.04.016.
[92] M. Krieg *et al.*, 'Atomic force microscopy-based mechanobiology', *Nat. Rev. Phys.*, vol. 1, no. 1, pp. 41–57, Jan. 2019, doi: 10.1038/s42254-018-0001-7.
[93] P. K. Mattila and P. Lappalainen, 'Filopodia: molecular architecture and cellular functions', *Nat. Rev. Mol. Cell Biol.*, vol. 9, no. 6, pp. 446–454, June 2008, doi: 10.1038/nrm2406.
[94] R. Capozza *et al.*, 'Cell Membrane Disruption by Vertical Micro-/Nanopillars: Role of Membrane Bending and Traction Forces', *ACS Appl. Mater. Interfaces*, vol. 10, no. 34, pp. 29107–29114, Aug. 2018, doi: 10.1021/acsami.8b08218.
[95] P. A. Yuya, D. C. Hurley, and J. A. Turner, 'Contact-resonance atomic force microscopy for viscoelasticity', *J. Appl. Phys.*, vol. 104, no. 7, p. 074916, Oct. 2008, doi: 10.1063/1.2996259.
[96] P.-A. Thorén *et al.*, 'Modeling and Measuring Viscoelasticity with Dynamic Atomic Force Microscopy', *Phys. Rev. Appl.*, vol. 10, no. 2, p. 024017, Aug. 2018, doi: 10.1103/PhysRevApplied.10.024017.
[97] K. P. Menard, *Dynamic Mechanical Analysis: A Practical Introduction, Second Edition*, 2nd edn. Boca Raton: CRC Press, 2008. doi: 10.1201/9781420053135.
[98] R. Garcia, C. J. Gómez, N. F. Martinez, S. Patil, C. Dietz, and R. Magerle, 'Identification of Nanoscale Dissipation Processes by Dynamic Atomic Force Microscopy', *Phys. Rev. Lett.*, vol. 97, no. 1, p. 016103, July 2006, doi: 10.1103/PhysRevLett.97.016103.
[99] P. Doležal, 'Korelace AFM a mikro-spektroskopie aplikovaná na soubor nanočástic', Feb. 2022, Accessed: July 21, 2025. [Online]. Available: https://dspace.cuni.cz/handle/20.500.11956/171632
[100] S. Kano, T. Tada, and Y. Majima, 'Nanoparticle characterization based on STM and STS', *Chem. Soc. Rev.*, vol. 44, no. 4, pp. 970–987, Feb. 2015, doi: 10.1039/C4CS00204K.
[101] I. Sychugov, A. Fucikova, F. Pevere, Z. Yang, J. G. C. Veinot, and J. Linnros, 'Ultranarrow Luminescence Linewidth of Silicon Nanocrystals and Influence of Matrix', *ACS PHOTONICS*, vol. 1, no. 10, pp. 998–1005, Oct. 2014, doi: 10.1021/ph500221z.
[102] 'Silicon Nanocrystals: Fundamentals, Synthesis and Applications | Wiley', Wiley.com. Accessed: Aug. 05, 2025. [Online]. Available: https://www.wiley.com/en-us/Silicon+Nanocrystals%3A+Fundamentals%2C+Synthesis+and+Applications-p-9783527629954

[103] M. Dasog, G. B. De los Reyes, L. V. Titova, F. A. Hegmann, and J. G. C. Veinot, 'Size vs Surface: Tuning the Photoluminescence of Freestanding Silicon Nanocrystals Across the Visible Spectrum via Surface Groups', *ACS Nano*, vol. 8, no. 9, pp. 9636–9648, Sept. 2014, doi: 10.1021/nn504109a.
[104] R. J. Clark *et al.*, 'From Hydrogen Silsesquioxane to Functionalized Silicon Nanocrystals', *Chem. Mater.*, vol. 29, no. 1, pp. 80–89, Jan. 2017, doi: 10.1021/acs.chemmater.6b02667.
[105] 'Enhanced FASP (eFASP) to Increase Proteome Coverage and Sample Recovery for Quantitative Proteomic Experiments | Journal of Proteome Research'. Accessed: Aug. 05, 2025. [Online]. Available: https://pubs.acs.org/doi/10.1021/pr4010019

8. Statement of the author's contribution to the publications

The publications [PI1], [PI2] were created during my postdoctoral stay in the laboratory of Prof. Jan Linnros, Ph.D., at KTH in Sweden. In both publications, I performed all measurements and conducted data analysis. Prof. I. Sychugov developed a theory to explain the narrow emission of the nanoparticles based on the thin shell theory, which was derived from my data analysis. I am the first author of the publication [PI2] in which I elucidate the chemical origin of the thin shell, explore in greater depth how the shell influences the linewidth of a Si nanoparticle, and confirm our earlier findings from publication [PI1]. Since I thought these results were patentable in 2016, I personally applied for a US patent under a grace period. I wrote and defended the patent, which was granted in 2019. The granting of this patent set a precedent for European scientists, who can now defend and apply for a patent by themselves and represent themselves in front of the US Patent Office. In publication [PI4], I measured the single dot spectra and contributed to the data analysis.

The papers in section B summarize our study of the interaction of nanoparticles with the biological environment, including cells. In paper [PI5], I was responsible for the zetapotential measurement and helped with the optical characterization. I helped to reveal that the nanoparticles are not fully oxidized. In paper [PI6], I was responsible for all the measurements except the AFM measurement and the LDH viability test. In the case of confocal microscopy, I assisted A. Broz; in the case of zeta-potential, I measured it under the supervision of Z. Bakaeva. I carried out all the analysis and wrote the paper. In paper [PI7], I was responsible for AFM and zetapotential measurement. I was also involved in the analysis of the data and theory development. In paper [PI8], I was responsible for the zetapotential measurement and wrote part of the article; at the same time, I contributed to the general discussion about the results (Investigation, Writing - review & editing). In papers [PI9] and [PI10], I helped to analyse and interpret the results. In addition, in article [PI10], I also characterized the nanoparticles' zeta potential. In publications [PI11], [PI12], [PI13], I was responsible for AFM measurement of the samples and helped to reveal the behaviour at the macroscale by looking at a biologically relevant nanoscale.

In summary, I am the first author of three publications and one patent in this collection, and I have contributed significantly to the remaining publications through both experimental work and data interpretation.

9. Appendix: Collection of publications